# SHAPE MODELS BASED ON ELLIPTIC PDES, ASSOCIATED ENERGIES, AND THEIR APPLICATIONS IN 2D AND 3D

A THESIS SUBMITTED TO
THE GRADUATE SCHOOL OF NATURAL AND APPLIED SCIENCES
OF
MIDDLE EAST TECHNICAL UNIVERSITY

BY

ASLI GENÇTAV

IN PARTIAL FULFILLMENT OF THE REQUIREMENTS
FOR
THE DEGREE OF DOCTOR OF PHILOSOPHY
IN
COMPUTER ENGINEERING

SEPTEMBER 2018

Approval of the thesis:

**SHAPE MODELS BASED ON ELLIPTIC PDES, ASSOCIATED ENERGIES, AND THEIR APPLICATIONS IN 2D AND 3D**

submitted by **ASLI GENÇTAV** in partial fulfillment of the requirements for the degree of **Doctor of Philosophy in Computer Engineering Department, Middle East Technical University** by,

Prof. Dr. Halil Kalıpçılar
Dean, Graduate School of **Natural and Applied Sciences** ______________

Prof. Dr. Halit Oğuztüzün
Head of Department, **Computer Engineering** ______________

Prof. Dr. Sibel Tarı
Supervisor, **Computer Engineering Department, METU** ______________

Prof. Dr. Tolga Can
Co-supervisor, **Computer Engineering Department, METU** ______________

**Examining Committee Members:**

Prof. Dr. Halit Oğuztüzün
Computer Engineering Department, METU ______________

Prof. Dr. Sibel Tarı
Computer Engineering Department, METU ______________

Assoc. Prof. Dr. Ali Devin Sezer
Institute of Applied Mathematics, METU ______________

Prof. Dr. Tolga Kurtuluş Çapın
Computer Engineering Department, TED University ______________

Assoc. Prof. Dr. Selim Aksoy
Computer Engineering Department, Bilkent University ______________

**Date:** ______________

**I hereby declare that all information in this document has been obtained and presented in accordance with academic rules and ethical conduct. I also declare that, as required by these rules and conduct, I have fully cited and referenced all material and results that are not original to this work.**

Name, Last Name: ASLI GENÇTAV

Signature :

# ABSTRACT

## SHAPE MODELS BASED ON ELLIPTIC PDES, ASSOCIATED ENERGIES, AND THEIR APPLICATIONS IN 2D AND 3D



Gençtav, Aslı
Ph.D., Department of Computer Engineering
Supervisor : Prof. Dr. Sibel Tarı
Co-Supervisor : Prof. Dr. Tolga Can



September 2018, 80 pages



By using an elliptic PDE or its modifications, we develop implicit shape representations and demonstrate their two- and three-dimensional applications. In the first part of the thesis, we present a novel shape characterization field that provides a local measure of roundness at each shape point. The field is computed by comparing the solution of the elliptic PDE on the shape domain and the solution of the same PDE on the reference disk. We demonstrate its potential via illustrative applications including global shape characterization, context-dependent categorization, and shape partitioning. In the second part, we solve the elliptic PDE multiple times varying either the diffusion parameter or the right hand side function and construct high-dimensional feature space. We then apply low-dimensional reduction to assign a distinctness value to each shape point. We use the obtained distinctness values for non-structural representation of two-dimensional shapes and saliency measurement of surfaces of three-dimensional shapes. In the third and the final part, we use the elliptic PDE modifications for bringing a pair of 3D shapes into comparable topology.

Keywords: Elliptic PDEs, Implicit Shape Representations, Shape Characterization, Shape Roundness

# ÖZ

## ELİPTİK KISMİ DİFERANSİYEL DENKLEM TABANLI ŞEKİL MODELLERİ, İLGİLİ ENERJİLER VE BUNLARIN 2 VE 3 BOYUTTAKİ UYGULAMALARI

Gençtav, Aslı
Doktora, Bilgisayar Mühendisliği Bölümü
Tez Yöneticisi : Prof. Dr. Sibel Tarı
Ortak Tez Yöneticisi : Prof. Dr. Tolga Can

Eylül 2018 , 80 sayfa

Bu tezde bir eliptik kısmi diferansiyel denklem veya modifikasyonları kullanılarak örtülü şekil temsilleri geliştirilmekte ve iki ve üç boyutlu uygulamaları gösterilmektedir. İlk bölümde her şekil noktası için yerel bir yuvarlaklık ölçümü sağlayan özgün bir şekil temsili sunulmaktadır. Bu temsilin hesabı için eliptik kısmi diferansiyel denklemin şekil üzerindeki çözümü ile yine aynı denklemin bir referans disk üzerindeki çözümü karşılaştırılmaktadır. Temsilin potansiyeli şeklin bütünsel karakterizasyonu, bağlama bağlı kategorizasyon ve şekil bölütleme gibi örnek uygulamalar ile gösterilmektedir. İkinci bölümde, ya difüzyon parametresi ya da sağ taraf fonksiyonu değiştirilerek eliptik diferansiyel denklem birçok kez çözülmekte ve yüksek boyutlu öznitelik uzayı oluşturulmaktadır. Sonrasında her bir şekil noktasına bir özgünlük değeri atamak üzere düşük boyuta indirgeme uygulanmaktadır. Elde edilen özgünlük değerleri iki boyutlu şekillerin yapısal olmayan temsili ve üç boyutlu şekillerin yüzeylerinin dikkati çekme ölçümü için kullanılmaktadır. Üçüncü ve son bölümde, bir çift 3B şekli karşılaştırılabilir topolojiye getirmek için eliptik kısmi diferansiyel denklem modifikasyonlarından yararlanılmaktadır.

Anahtar Kelimeler: Eliptik Kısmi Diferansiyel Denklemler, Örtülü Şekil Temsilleri, Şekil Karakterizasyonu, Şekil Yuvarlaklığı

*To my dear husband*

# ACKNOWLEDGMENTS

Foremost, I would like to express my sincere gratitude to my advisor Prof. Dr. Sibel Tarı for her continuous support and guidance throughout this study. As her student, I have always felt very lucky. She is such a unique and rare mentor knowing the art of loving. The experiences that I went through with the help of her encouragement and support improved me a lot.

I would like to thank my co-advisor Prof. Dr. Tolga Can and the members of the jury Prof. Dr. Halit Oğuztüzün, Assoc. Prof. Dr. Ali Devin Sezer, Prof. Dr. Tolga Kurtuluş Çapın and Assoc. Prof. Dr. Selim Aksoy for their encouraging and insightful comments. I specially thank Prof. Dr. Halit Oğuztüzün for sharing his wisdom by giving advices at important times.

My sincere thanks are for my dear husband Murat. This thesis would not be possible without his support and love.

I am grateful to my family for always being with me.

I gratefully acknowledge the support of The Scientific and Technological Research Council of Turkey (TUBITAK) under program 2211/C scholarship and under grant 112E208.

## TABLE OF CONTENTS

## LIST OF TABLES

TABLES

## LIST OF FIGURES

FIGURES

## LIST OF ABBREVIATIONS

| | |
|---|---|
| PDE | Partial Differential Equation |
| 2D | 2 Dimensional |
| 3D | 3 Dimensional |
| EDT | Euclidean Distance Transform |
| RPCA | Robust Principal Component Analysis |
| t-SNE | t- Distributed Stochastic Neighbor Embedding |

# CHAPTER 1

# INTRODUCTION

Analyzing shapes of objects has been of great importance in many areas such as medicine, materials science, industrial processes, computer vision, object recognition, 3D printing and computer graphics. In [30], it is stated that computational tools for the analysis of cell shape are increasingly necessary. In [32], an image processing computer procedure is proposed for the characterization of the shape of the graphite particles in ductile cast iron since the mechanical performances of the ductile cast iron depend on the difference of the shape of the graphite particles from a perfect sphere. In [3], two new measures are presented for the characterization of pharmaceutical micro particles using image analysis techniques with the aim of characterization and monitoring of pharmaceutical pelleting processes. Shape analysis plays an important role in computer vision systems involving object recognition since the shape is the only attribute which enables recognizing an object without its other attributes such as color or texture. In [44], a perceptual model for determining 3D printing orientations is proposed where the considered metrics, namely, area of support, visual saliency, preferred viewpoint, and smoothness preservation, involve shape analysis. Finding correspondence between a pair of 3D models via analyzing their shapes is a prerequisite for several computer graphics applications such as morphing, interpolation, attribute transfer.

Analysis of shapes highly depends on their representation. One class is composed of landmark-based representations utilizing landmark or interest points that can be easily identified and compared across individual shapes. Unfortunately, these representations are not suitable for every shape since unequivocal and stereotyped landmark points can not be afforded by all shapes. There are boundary-based represen-

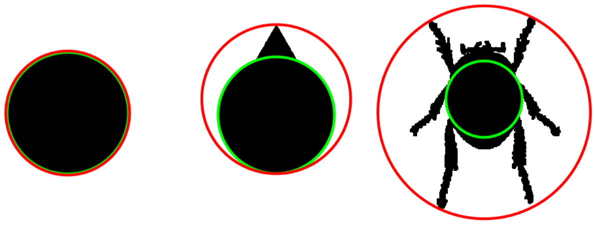

Figure 1.1: Maximal inscribed circle (green) and minimal circumscribing circle (red) for three different shapes.

tations which model the shape boundary in terms of points, splines or parameterized curves. However, they fail to capture two-dimensional shape features such as necks and protrusions. Another class of representation includes skeleton-based representations which model the shape interior via local symmetry axis called skeleton. These representations have been proven to be useful for modeling the shape structure. However, their extraction and matching are challenging tasks. Finally, there are implicit representations or fields which map the shape interior to the real line $\mathbb{R}$ and contain high-level information resulting from short-range and long-range interactions between the shape points. One example in this class is Euclidean Distance Transform (EDT) of the shape which assigns each point to its distance to the nearest boundary point. The level curves of the EDT emulate motion of the shape boundary in such a way that each point on it moves with a unit speed in the direction of the inward normal. The EDT implicitly codes the shape structure but it is not straightforward to extract this information. Another example for the implicit representations is the part-coding field [38] which provides a hierarchical partitioning of the shape domain into meaningful parts by incorporating local and global shape information.

In this thesis, we promote implicit representations which provide richer information. Consider the case of measuring shape roundness. One way is to extract and utilize global shape properties such as the maximal inscribed circle or the minimal circumscribing circle of the shape (see Figure 1.1) to reach a single global measure of roundness. For example, it can be defined as the size ratio between the maximal inscribed circle and the shape or the size ratio between the shape and the minimal circumscribing circle. In this thesis, we follow an alternative approach where we construct an implicit representation by measuring roundness at each shape point locally. In Chap-

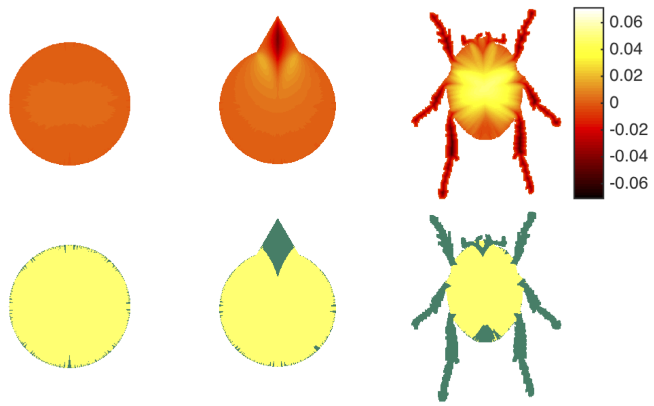


Figure 1.2: Discrepancy for the shapes in Figure 1.1 (top) and their partitioning according to discrepancy sign (bottom).

ter 2, we present a novel field called discrepancy which measures deviation of local configuration of each shape point from a reference disk. In Figure 1.2 (top), we show discrepancy for three different shapes. For a perfect disk, discrepancy is uniformly zero and hence distribution of the field values is the impulse function with 0 entropy. As the shape diverges from a disk, discrepancy attains the highest positive values on central regions and the lowest negative values on periphery which leads to an increase in the entropy. Discrepancy is a rich representation providing natural binary partitioning of the shape domain into central and peripheral regions via simple thresholding (see Figure 1.2 (bottom)). As presented in § 3.1 of Chapter 3, entropy of positive and negative discrepancy values provides a global characterization for body roundness and peripheral thickness uniformity.

## 1.1 General Framework of Thesis

The methodologies and derivations presented in this thesis are based on the following elliptic Partial Differential Equation (PDE) and its modified versions.

Let the shape $S$ be an open connected bounded set with boundary $\partial S$.

$$\left(\Delta - a^2\right) v = 0 \text{ subject to } v\Big|_{\partial S} = 1 \tag{1.1}$$

where $\Delta$ is the Laplace operator, $\frac{\partial^2}{\partial x^2} + \frac{\partial^2}{\partial y^2}$ in 2D and $\frac{\partial^2}{\partial x^2} + \frac{\partial^2}{\partial y^2} + \frac{\partial^2}{\partial z^2}$ in 3D, and $a$ is a scalar parameter. This PDE has been successfully employed in shape analysis in approximating curvature dependent shape evolution and skeleton computation [40]. The solution of (1.1) minimizes the following energy which can be proven using calculus of variations, namely, Euler-Lagrange equation.

$$\arg\min_v \int_S \left( |\nabla v|^2 + a^2\, v^2 \right) \mathrm{d}s \text{ subject to } v\Big|_{\partial S} = 1 \tag{1.2}$$

The parameter $a$ determines smoothness of the level curves of the solution field, $v$, inversely. Here smoothness is not used in the smoothness of the function in the mathematical sense, i.e., in the sense of differentiability class of the function. Instead, it is used in the sense that the level curves are getting less detailed and rounder. Of course, the total derivative or some differential property along the level curve (e.g. curvature) is decreasing. This usage (which is also related to low pass filtering or denoising) is common in shape and image analysis.

In Chapter 4, we consider $(1 - v)$ instead of $v$ whose associated energy is

$$\arg\min_v \int_S \left( |\nabla(1 - v)|^2 + a^2\, (1 - v)^2 \right) \mathrm{d}s \text{ subject to } (1 - v)\Big|_{\partial S} = 1 \tag{1.3}$$

which is equivalent to

$$\arg\min_v \int_S \left( |\nabla v|^2 + a^2\, (1 - v)^2 \right) \mathrm{d}s \text{ subject to } v\Big|_{\partial S} = 0. \tag{1.4}$$

Notice that the minimizer of (1.4) is a smooth approximation of the characteristic function which is 1 on the shape domain and 0 elsewhere. The minimizer of (1.4) can be obtained via solving the following PDE.

$$(\Delta - a^2)\, v = -a^2 \text{ subject to } v\Big|_{\partial S} = 0 \tag{1.5}$$

In Chapter 4, we solve the following PDE by scaling the right hand side of (1.5), which only scales range of the values leaving geometry of the level curves intact.

$$(\Delta - a^2)\, v = -1 \text{ subject to } v\Big|_{\partial S} = 0 \tag{1.6}$$

In Chapters 5 and 6, we consider the following energy

$$\arg\min_v \int_S \left( |\nabla v|^2 + a^2\, (v - f)^2 \right) \mathrm{d}s \text{ subject to } v\Big|_{\partial S} = 0 \tag{1.7}$$

and obtain its minimizer via solving the following PDE

$$(\Delta - a^2)\, v = -f \text{ subject to } v\Big|_{\partial S} = 0. \tag{1.8}$$

This way, we obtain a smooth approximation of an external function $f$ that we choose.

The details for numerical implementation of the PDEs (1.1), (1.6), and (1.8) are given in Appendix A.1.

## 1.2 Contributions

Our main focus in this thesis to devise implicit shape representations incorporating local and global shape information and utilize them for the problems related to analysis of 2D and 3D shapes. In particular, this thesis makes the following contributions:

- A novel shape characterization field measuring deviation of local configuration of each shape point from a reference disk is presented. The new field called discrepancy is computed indirectly by comparing the solution of an elliptic PDE on the shape domain and the solution of the same PDE on the reference disk. The potential of discrepancy is demonstrated via three different applications which are global characterization of the body roundness and periphery thickness uniformity, context-dependent categorization, and binary shape domain labeling.

- A non-structural shape representation that is robust to transformations such as translation, rotation, scaling and motion of limbs or independent motion of parts called articulations is presented. The pairwise shape similarity measure computed using the proposed representation is used to cluster a set of 2D shapes. A performance comparable to state of the art methods is achieved without modeling the shape structure in the form of graphs or trees.

- A non-local saliency measure defined on surfaces of 3D shapes is presented. Local to global shape information is integrated by the measure during both high-dimensional feature computation and low-dimensional reduction via Robust Principal Component Analysis (RPCA).

- A previous method [16] for equating topologies of 3D shapes for the purpose of finding their correspondence is improved.

## 1.3 Thesis Organization

In Chapters 2 and 3, we present discrepancy and three applications of it, respectively. In both of Chapters 4 and 5, we employ high-dimensional feature extraction and low-dimensional reduction via RPCA. In Chapter 4, we present a non-structural shape representation for articulated shapes. In Chapter 5, we present a non-local measure of mesh saliency. In Chapter 6, we present a method for bringing a pair of 3D shapes into comparable topology. Finally, in Chapter 7, we provide summary and conclusion.

# CHAPTER 2

# DISCREPANCY - LOCAL/GLOBAL SHAPE CHARACTERIZATION WITH A ROUNDNESS BIAS

In this chapter, we present a novel shape characterization tool called discrepancy which measures deviation of local configuration of each shape point from a reference disk. Discrepancy is a local property biased by the global shape as it is computed locally at each shape point and the radius of the reference disk is determined globally as the radius of the maximal inscribed circle of the shape. Discrepancy is computed indirectly by comparing the solution of the PDE (1.1) on the shape domain and the solution of the same PDE on the reference disk. For each point of the shape domain, the corresponding point in the reference disk is determined based on the distance to the nearest boundary.

The chapter is organized as follows. In § 2.1, we present the motivation behind the proposed shape characterization tool along with its intuitive idea. In § 2.2, a brief review of the related work is given. In § 2.3, the details of discrepancy are provided.

## 2.1 Motivation and Intuitive Idea

In the field of shape characterization, in one end of the spectrum are the structural descriptors in the form of part hierarchy trees or skeleton graphs extracted from distance transforms. They have been successfully employed in characterizing shapes with well defined part hierarchy with semantically meaningful parts, e.g. a horse shape. In the other end of the spectrum are the global descriptors such as moments and specialized descriptors derived from moments, which may be better suited for shape collections that lack certain analytical hierarchy and as well as strong semantic meaning for either

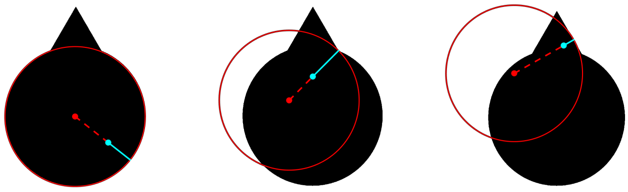


Figure 2.1: The imaginary reference disk at three distinct shape points marked via cyan dot in (a)-(c).

within the collection or within a particular member of the collection.

In this chapter, we present an alternative characterization equally suitable for shapes of both types. In the presented scheme, a shape is modeled via a field defined on the entire shape domain where the field value is calculated locally using a reference shape and a global parameter. Specifically, the reference shape is a disk and the global parameter is the radius of the disk. The intuitive idea is to measure (at each shape location) the deviation of the local configuration from the reference shape. We call this field as *discrepancy*. If the shape is a perfect disk, discrepancy is uniformly zero.

Disk shape frequently appears as a reference in shape characterization applications since it has a simple form with fundamental properties such as compactness, convexity, isotropy, uniformity of distance from boundary to center, uniformity of boundary curvature and etc. Different from the global shape measures that assign a single scalar value to a given shape, discrepancy provides richer information where it attains a value at each point of the shape domain. When necessary global measures can be calculated using the field values.

The novel feature of our proposed scheme is that we calculate deviation from the reference disk indirectly using the solution of (1.1) computed for both the shape and the reference disk.

The intuitive idea is explained in Figure 2.1. Consider a disk with a triangular protrusion on top. In Figure 2.1 (a)-(c), the cyan dot shows a domain point. In each case, an imaginary circle (red) which is tangent to the nearest boundary point and with the radius $A$ equal to the radius of the maximal inscribed disk is drawn.

The first location, cyan dot shown in (a), is away from the triangular protrusion, its local circle coincides with the maximal inscribed circle. The second location, cyan dot shown in (b), is still inside the disk but in the upper half closer to the protrusion. The third location, cyan dot shown in (c), is in the protruding region. The cyan line segment measures the distance $d$ between the point and its nearest boundary point. Notice that $A - d$ is the distance from the disk center to the cyan dot's location. Discrepancy at each shape point is computed as the difference between the value of the solution of (1.1), and the value that the solution of (1.1) would take on a disk point located at the radial distance $A - d$. That is discrepancy is a local property biased by the global shape.

## 2.2 Related Work

In [45], a global measure of circularity is derived using a geometric moment invariant of a disk shape and it is utilized in image processing tasks from medical, industrial and astronomical applications. As any ellipse can be obtained by applying an affine transform to a disk, an ellipticity measure is presented in [31] using an affine moment invariant of a disk shape where a highest possible ellipticity is assigned to all the ellipses, including circles. In [2], a family of ellipticity measures which distinguishes among ellipses of different aspect ratios is defined and applied to the galaxy classification problem. A generalization of moment based circularity and ellipticity measures is presented in [28] so that they can be applied to higher dimensional data. A probabilistic approach is followed in [20] to obtain a circularity measure which is not affected by discrete resolution, region overlaps or noisy/partial boundary.

## 2.3 Discrepancy

Let the shape $S$ be an open connected bounded set with boundary $\partial S$. Let $v : S \to R$ be a mapping governed by the PDE (1.1). The solution to (1.1) can be easily calculated with numerical methods. A sample $v$ function is depicted in Figure 2.2 (a).

Due to the selected uniform inhomogeneous boundary condition, $v$ attains the highest value $1$ at $\partial S$ and decays towards the interior regions.

Now let us consider the same equation on $\Omega$, an open disk of radius $A$, with boundary $\partial\Omega$. The solution can be obtained either numerically or analytically. Due to rotational symmetry of $\Omega$ and the uniform boundary condition in (1.1), the solution $v$ depends only on the radial distance and can be expressed as $v(r, \theta) = I_0(ar)/I_0(aA)$. Here, $r$ and $\theta$ correspond to polar coordinates and $I_0$ denotes the zeroth order modified Bessel function of the first kind. The details can be found in [17].

Now, let $S$ be a shape with the maximal inscribed circle of radius $A$. Let us denote the solution of (1.1) for $S$ as $v_S$, and $v^\Omega$ to denote the solution for the disk of appropriate radius. If the shape $S$ happens to be a disk, then we can speak of $v^\Omega - v_S$ which is zero up to a numerical accuracy. Suppose the disk is perturbed via a small triangular appendage (previously shown in Figure 2.1). Imagine the maximal inscribed circle in $S \cup \partial S$. Except for its small fragment, it will coincide with $\partial S$. On the small fragment, the solution $v_S$ will be smaller than $1$, decaying further towards the fragment center. Now, one can imagine a new disk with a non-uniform boundary condition. Inside this new disk, because the propagated values from the boundary are lower than $1$ at certain angles (direction of the triangular appendage), the realized solution becomes lower than $v^\Omega$ under the assumption of uniform boundary condition.

As $S$ deviates more and more from disk, discrepancy will diverge more and more from the zero. The question is how to calculate discrepancy for points in $S$ that do not coincide with the points in $\Omega$. That is we need an ability to produce an estimate of $v^\Omega$ at those domain points falling out of the imaginary inscribed circle. Toward this end, we may utilize for each point $p$, its minimal distance $d(p)$ to $\partial S$ and consider $v^\Omega$ at the radial distance $A - d(p)$. This is equivalent to imagining a local scenario where the point is at radial position $A - d(p)$ in polar coordinates centered at the center of a putative circle of radius $A$ passing through the nearest boundary point of $p$. Notice that $0 \leq d(p) \leq A$ for all $p \in S$. Let $v^{S \to \Omega}$ denote $v^\Omega$ extended to entire $S$, then

$$v^{S \to \Omega}(p) = v^\Omega \text{ at the radial distance } (A - d(p)) \tag{2.1}$$

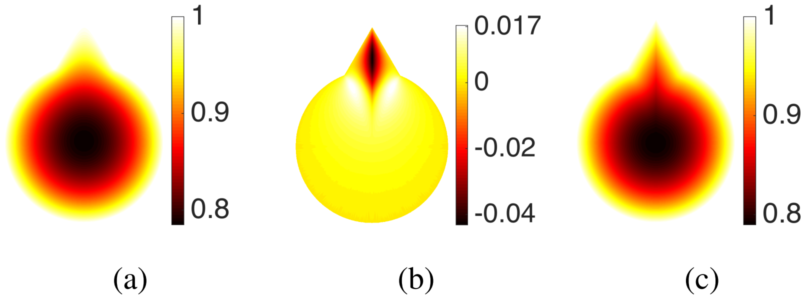


Figure 2.2: Illustration for the disk with an appendage. (a) $v_S$ (b) Discrepancy. (c) $v^{S \to \Omega}$ which is $v^{\Omega}$ extended to the shape domain $S$.

Consequently, discrepancy is

$$D(p) = v^{S \to \Omega}(p) - v_S(p) \tag{2.2}$$

If $p$ happens to be on an appendage considerably narrower as compared to thickest part, such as the case in Figure 2.1 (c), $v^{S \to \Omega}(p)$ will be lower than $v_S(p)$. This is because $v_S(p)$ depends on the values propagated from the shape boundary (mainly the boundary of the appendage) whereas $v^{S \to \Omega}(p)$ depends on the values propagated from the boundary of the imaginary circle associated with the point. As the point is closer to the shape boundary compared to the boundary of its associated imaginary circle, $v_S(p)$ is higher than $v^{S \to \Omega}(p)$. In contrast, in the innermost parts, as discussed before, $v^{S \to \Omega}(p)$ will be higher than $v_S(p)$.

If the shape is a disk with an appendage or protrusion, then it is expected that discrepancy on the appendage or protrusion will be negative whereas on an inscribed central disk positive. An illustration on the disk with an appendage is in Figure 2.2.

We note that $-1 < D(p) < 1$ for all $p \in S$ since $0 < v^{S \to \Omega}(p) < 1$ and $0 < v_S(p) < 1$ for all $p \in S$.

### 2.3.1 Illustrative Results

In Figure 2.3, illustrative discrepancy examples for 5 shapes from MPEG-7 dataset [21] are depicted. The highest positive values are attained on central regions whereas the lowest negative values on appendages, protrusions and boundary detail. For the three

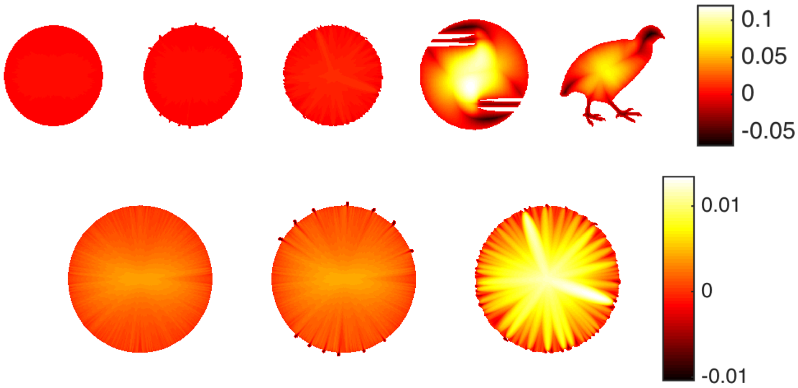


Figure 2.3: The highest positive values are attained in central regions whereas the lowest negative on the appendages, protrusions and boundary detail. The bottom row depicts the first three shapes only. As seen in the color-bar, the range of discrepancy for the three disks is quite low.

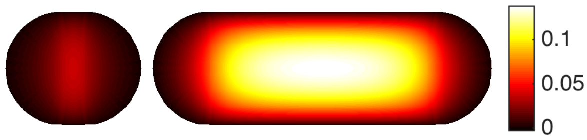


Figure 2.4: Discrepancy for two rods of varying length.

disks, discrepancy values are very close to zero. The case of disks are redisplayed at the bottom row where the dynamic range of the display is adjusted for improved visibility. Observe that placing regular circular bumps (middle) is less disturbing than irregular notching (right). The anisotropy of discrepancy in the later case is a consequence of non-uniform notching. The brighter central region of discrepancy extends towards the two deepest notches at approximately $120°$ and $-30°$.

For an arbitrary shape, discrepancy takes both positive and negative values. However, for a perfect rod obtained by rolling a disk, all values are positive (see Figure 2.4). The maximum value of discrepancy increases as the rod length increases.

### 2.3.2 Entropy

For a perfect disk, discrepancy is uniformly zero, hence, discrepancy histogram is a scaled impulse. Consequently, the entropy is zero. If we add some noise, the entropy increases. Even for a noisy disk, the interior region with small positive discrepancy is significantly larger than the exterior region with negative discrepancy. If we add a smaller round piece on top of the disk (e.g. the handle of a pocket watch), the exterior region grows in size significantly contributing to an increase in the entropy. If, however, we make a hole in the handle to change the round handle to a ring of uniform thickness, two noteworthy effects are observed. First, the exterior region gets smaller. Second, the *negative* discrepancy distribution over the exterior region becomes more uniform. Note that discrepancy is a function of distance to boundary. Hence, discrepancy distribution over the ring of constant thickness has a lower variance compared to that over a disk of the same radius. Hence, the entropy decreases. If we consider putting together two disks of the same size, then both the size of exterior region and the overall entropy will decrease as compared to the size of the exterior region and the overall entropy obtained when the disks are of different size. The entropy in the interior region, however, may increase. This is because the interior region, depending on the neck thickness, may become more like a dumbbell rather than a disk.

### 2.3.3 Implementation Details

The distance transform is computed using the available Matlab command, which is an implementation of the method in [27]. $A$ is obtained as the maximum value of the distance transform.

The only parameter, $a$, is inversely related to the diffusion (smoothing radius). Hence, we take it on the order of the shape radius, *i.e.*, we set it to $1/A$. As the diffusion level increases, the range of discrepancy decreases. Nevertheless, after level $A$, the overall pattern stabilizes. Hence, increasing diffusion level further becomes unnecessary. The illustrations in Figure 2.5 and Figure 2.6 also offer an experimental justification for fixing the value $A$ as the diffusion level. In Figure 2.5, we present statistics of discrepancy computed at six different choices of $a$ for the input shapes shown in (d).

Variation of the input shapes is due to the lower disk, which gradually increases in size and approaches to the upper disk. Notice that the reference shape (the maximal inscribed disk) remains the same for all input shapes. The maximum (positive) value of discrepancy, which results from the fact that the upper disk is a discretization of the reference shape, approaches to $0$ as the diffusion level (1/$a$) increases. The minimum (negative) value of discrepancy, which is due to the difference between the lower disk and the reference shape, shows a smoother change as the diffusion level increases. Notice that the minimum value of discrepancy first decreases then increases, which means that the lower disk is considered as a noise until it becomes comparable to the reference shape. Discrepancy entropy computed using the default bin size $0.001$ shows compatible behavior for the different choices of $a$ except $1/(0.2A)$ and $1/(0.1A)$ corresponding to very small diffusion levels. As evident in Figure 2.6, increasing the level from $A$ to $A^2$ does not bring further change to the pattern.

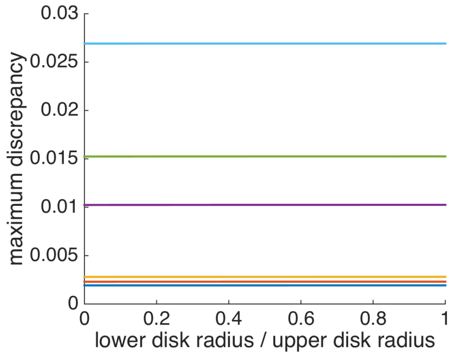


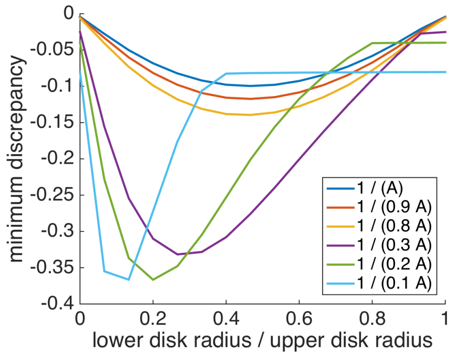


(a) (b)

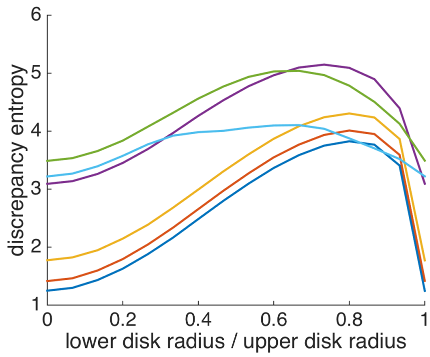


(c)

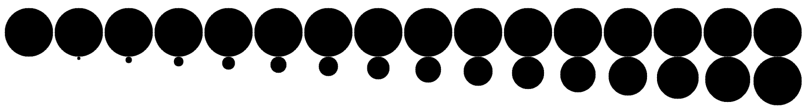

(d)

Figure 2.5: (a)-(c) Statistics of discrepancy at $6$ different choices of $a$: $1/(A)$, $1/(0.9\,A)$, $1/(0.8\,A)$, $1/(0.3\,A)$, $1/(0.2\,A)$, and $1/(0.1\,A)$. (d) Input shapes associated with x-axis.

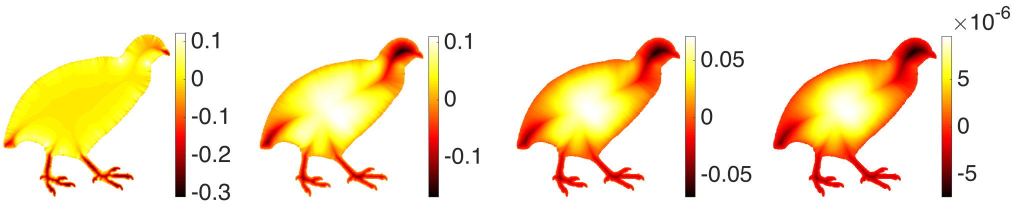


Figure 2.6: Discrepancy for increasing values of $a$. From left to right, $a = 1/(0.1\,A)$, $a = 1/(0.5\,A)$, $a = 1/A$, and $a = 1/A^2$.

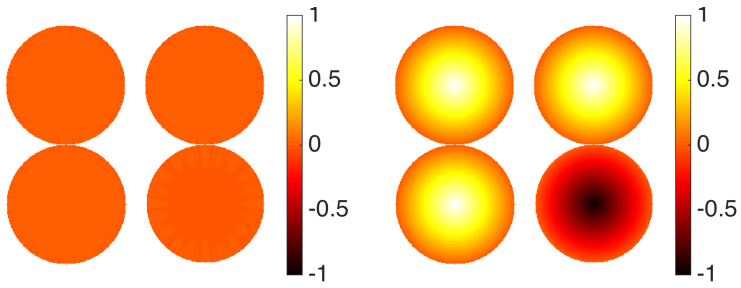


(a) (b)

Figure 2.7: (a) Discrepancy. (b) Signed distance with respect to maximal inscribed circle(s).

### 2.3.4 Signed Distance with Respect to Maximal Inscribed Circle(s) versus Discrepancy

Discrepancy behaves quite different than a signed distance field where the distances are calculated with respect maximal inscribed circle(s). The signed distance takes positive/negative values inside/outside maximal inscribed circle(s) where we linearly normalize the distances to have the maximum value of 1. The most obvious deficiency of any construction with reference to maximal inscribed circle(s) is the lack of representational stability. For example, consider a combination of two disks as in Figure 2.7. In the first case, the disks have the same radius hence there are two maximal inscribed circles. In the second case, the radius of the lower disk is reduced just by 1 pixel, which is approximately $1 - 2\%$. We see that the signed distance shows an abrupt change against a small difference whereas the discrepancy field exhibits a robust behavior.

# CHAPTER 3

# APPLICATIONS OF DISCREPANCY

In this chapter, we present three applications of discrepancy presented in the previous chapter. In § 3.1, we illustrate that the distribution entropy can be used for global characterization of the body roundness and periphery thickness uniformity. In § 3.2, we demonstrate the potential of discrepancy histogram as a feature in context-dependent categorization and sub-categorization tasks. In § 3.3, we show that discrepancy provides a natural binary partitioning of the shape domain.

## 3.1 Application-1: Entropy-based Ordering

In the experiments, entropy values are calculated separately over the positive and the negative discrepancy values, and then the shapes are ordered with respect to increasing mean entropy. The probability distribution of discrepancy values is obtained by constructing their histogram with a constant bin size and normalizing the histogram sum to 1. We compute discrepancy histogram by dividing the range $[-1, 1]$, which contains all possible values of discrepancy, into bins of equal size, and counting the number of shape pixels falling inside each bin. Default bin size is set $0.001$.

In Figure 3.1, we present the entropy based ordering of the shapes from the beetle and the device-2 categories of MPEG7 dataset [21]. Considering the beetle shapes, the entropy decreases with respect to roundness of the body and uniformity of the peripheral limbs. Considering the device-2 shapes, the entropy increases as the central region shrinks and the branch thickness becomes comparable to the central region thickness, which means divergence from a disk. Considering both of the orderings, we see that the shapes in the same sub-category are in consecutive order in spite of

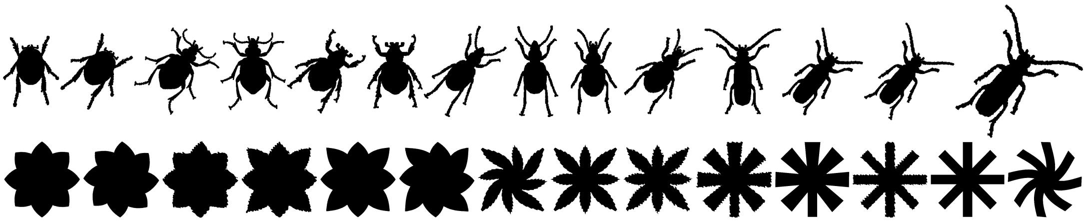

Figure 3.1: Entropy order.

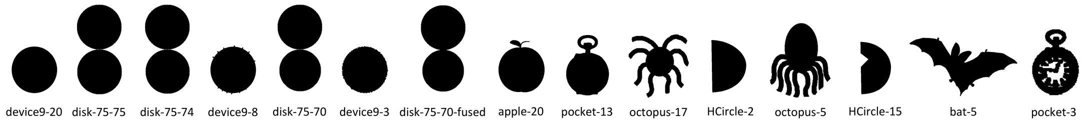


(a) Discrepancy

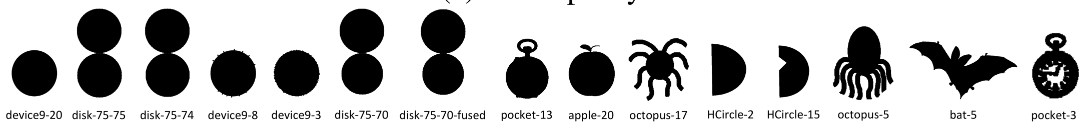


(b) Discrepancy (bin size $0.01$)

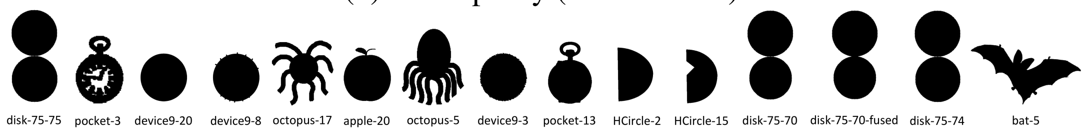


(c) Signed Distance

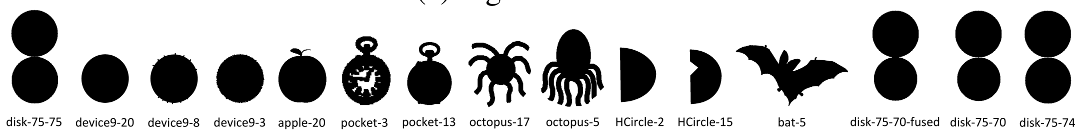


(d) Signed Distance (bin size $0.01$)

Figure 3.2: Entropy order.

the variations due to rotation, scaling, antenna/leg crops, boundary noise addition, and branch bending.

In Figure 3.2, we present the entropy ordering of sample shapes using discrepancy and the signed distance (see § 2.3.4) where sensitivity to the bin size is illustrated by employing a different selection ($0.01$). First, consider the ordering in Figure 3.2 (a) for which discrepancy is used with the default bin size. As expected, the entropy is smaller for the first seven shapes, which are composed of three versions of a disk (a plain one, one with circular bumps, and one with boundary notching) and four pairwise combinations of disks with the same or slightly different radius weakly connected or fused. Adding peripheral parts to a circular shape increases the entropy as in the case of the apple, the pocket, and the octopus. The entropy increases when the octopus has an elliptic body rather than a circular one. The half circle is far from being round and the entropy further increases when it is notched. The entropy is high for the pocket and the bat shapes both of which have details of varying thickness. We observe that the entropy ordering is robust to the change of the bin size when discrepancy is employed (see Figure 3.2 (a)-(b)). Flips occur between consecutive shapes but the essential ordering is preserved. For example, the first seven shapes composed of disks keep preceding the other shapes, the shapes formed via attaching peripheral parts to a circular body keep succeeding the disks, and etc. Now, consider the ordering in Figure 3.2 (c) obtained using the signed distance. The representational instability of the signed distance is observed in the ordering as the pairwise combinations of disks with slightly different radius are far from the combination with the identical disks. In Figure 3.2 (c)-(d), we see that there are significant differences between the two orderings and hence the entropy ordering is sensitive to the bin size when the signed distance is employed. For example, the detailed pocket precedes the three disks in the first ordering whereas it succeeds them in the second one or the octopus shapes precede one of the disks in the first ordering whereas they succeed all of the disks in the second one.

## 3.2 Application-2: Grouping

Both the range and the distribution of discrepancy depend on the complex way the shape deviates from a disk. In particular, we expect that discrepancy distribution to be a good property and the difference between a pair of distributions to be a good measure of dissimilarity.

We perform illustrative context-dependent grouping experiments using discrepancy histogram as the only shape property to calculate pairwise distances. Since the purpose of our experiments is to give a proof of concept, we employ only a single property (histogram) and use the $L^1$ distance between two histograms as pairwise shape dissimilarity measure.

In order to define the pair-wise histogram distance, we first construct normalized discrepancy histograms as described in § 3.1 and we then compute the sum of the absolute value of the bin-wise differences.

Let the number of shapes in the collection be $n$. We represent each shape using an $n$-vector of which components denote pairwise histogram distances between the respective shape and all the $n$ shapes in the collection. To observe grouping effect, we map all $n$ $n$-dimensional feature vectors to a plane. For this purpose we use t-Distributed Stochastic Neighbor Embedding (t-SNE) [41] which aims to model each object by a two- or three-dimensional point in such a way that similar objects are modeled by nearby points whereas dissimilar objects are modeled by distant points. Each of the $n$ shapes can then be visualized as a point in the plane.

We conduct two distinct groups of experiments. In the first, the input set is composed of the shapes from a single category. That is we focus on *fine-grained* categorization. In the second, we explore the robustness of discrepancy histogram with respect to visual transformations including extreme articulations. We focus on context dependent category characterization, starting with a small number of categories and then gradually increasing the number.

In the grouping experiments, we consider smoothed versions of discrepancy as well as its non-smoothed version. The smoothing is performed at two different levels via diffusion of discrepancy with homogeneous Neumann boundary condition where the diffusion time is chosen as $(0.5A)$ and $(0.5A)^{1/2}$. This is equivalent to convolving discrepancy with the Gaussian of standard deviation $\sigma = \mathcal{O}(A^{1/2})$ and $\sigma = \mathcal{O}(A^{1/4})$.

**Shapes from a single category.** We performed two experiments using respectively the device-2 and the beetle categories of the MPEG-7 data set [21]. Each of the two categories contains 20 instances.

The results are presented in Figures 3.3 and 3.4, respectively. The device-2 category contains plain, chiral and noisy versions of the some basic shapes, naturally forming several equivalence classes serving as fine-grained sub-categories. Likewise, the beetle category contains instances obtained via scaling, rotation, boundary noise addition or antenna/leg crops. To emphasize these sub-categories, we highlight the respective

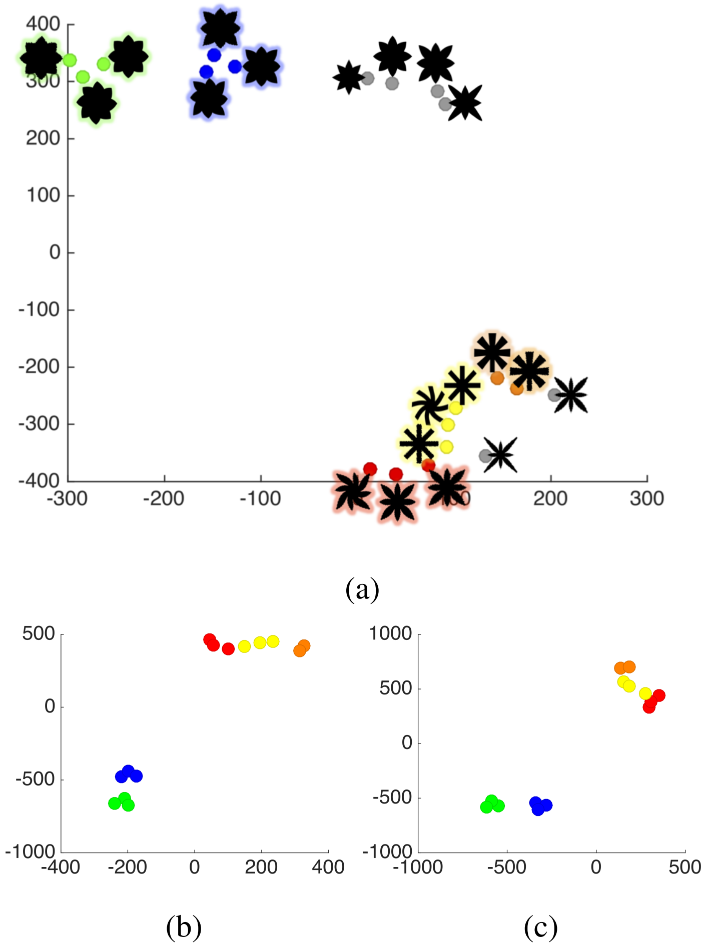


Figure 3.3: Grouping of the device-2 shapes using discrepancy histogram. Discrepancy is smoothed at different levels. In the last result, no smoothing is applied.

instances using the same color. Note that scale normalization is employed for better visualization of the grouping results. True scales of the shapes, however, are preserved during the experiments. In Figure 3.4 (d), we exemplify the transformations by presenting sample shapes in their true scales.

Observe that discrepancy (whether it is smoothed or not) is robust to these transformations since the shapes highlighted with the same color are positioned very close to each other. Considering the groupings in Figure 3.3, we see that the shape set is divided into two coarse groups: the shapes with a larger center and short protrusions are on one side whereas the shapes with a smaller center and long prevailing branches are on the other. Considering the groupings in Figure 3.4, we see that the beetle shapes

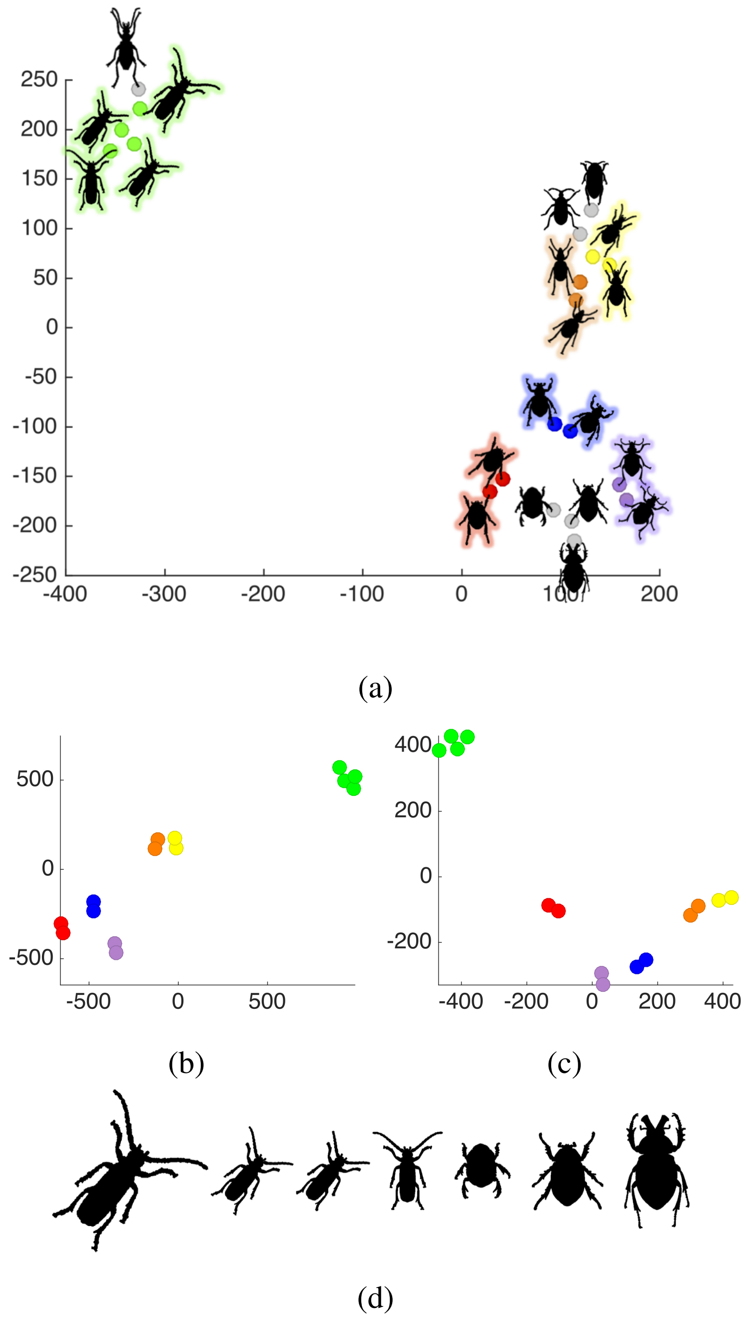


Figure 3.4: (a)-(c) Grouping of the beetle shapes using discrepancy histogram. Discrepancy is smoothed at different levels. In the last result, no smoothing is applied. (d) Sample shapes in their true scales.

are grouped according to the form of their body which is highly elongated for the shapes on one corner whereas it is composed of more circular regions for the shapes on the other side. We obtain similar grouping results when no smoothing is applied (shown in (c)) or discrepancy is smoothed with the Gaussian of standard deviation $\sigma = \mathcal{O}(A^{1/2})$ (shown in (a)) or $\sigma = \mathcal{O}(A^{1/4})$ (shown in (b)).

**Multi category context dependent grouping.** We perform a sequence of grouping experiments using the shapes shown in Figure 3.5. There are 7 categories each with 20 instances, taken from the dataset in [10]. Notice that there are significant variations between the shapes of the same category in terms of their scale and position of their articulations.

First, we consider the first 60 shapes in the elephant, the hand and the human categories. We obtain a grouping result in which the three categories are clearly separated from each other (see Figure 3.6 (a)). We observe that the distinctness between the categories is captured by discrepancy histogram despite the variation of the shapes with respect to their scale and articulations. In Table 3.1, we present the extrema of discrepancy. Observe that the maximum discrepancy decreases as the central region becomes rounder. For example, among the three categories, the maximum discrepancy is smaller for the hand shapes which have a circular palm in contrast to the elongated body of the human and the elephant shapes. Also, observe that the absolute value of the minimum discrepancy decreases as the limb to body thickness ratio becomes smaller. These observations are consistent with our expectation since the limiting case would be a disk shape (a perfect circle with no limbs) for which discrepancy is 0.

Next, we add 40 more shapes from the cat and the face categories extending the set to include 5 categories with the total of 100 shapes. Considering the body and limbs, the cat shapes can be regarded as similar to the elephant shapes. Considering the lack of protrusions, the face category appears *significantly* separate from the remaining four. The grouping result shown in Figure 3.6 (b) is consistent with our expectation since the cat shapes are clustered close to the elephant shapes and the face shapes form a new group far from the other clusters. If we include the horse category in the shape set, we see that the horse shapes are grouped in the vicinity of the elephants and the

Table 3.1: The range of discrepancy smoothed with the Gaussian of standard deviation $\sigma = \mathcal{O}(A^{1/2})$ for 8 different shape categories.

| | max discrepancy mean $\pm$ std | min discrepancy mean $\pm$ std |
|---|---|---|
| human | $0.101 \pm 0.010$ | $-0.037 \pm 0.001$ |
| hand | $0.066 \pm 0.008$ | $-0.033 \pm 0.002$ |
| elephant | $0.110 \pm 0.012$ | $-0.033 \pm 0.003$ |
| cat | $0.114 \pm 0.014$ | $-0.032 \pm 0.002$ |
| face | $0.086 \pm 0.006$ | $-0.015 \pm 0.002$ |
| ray | $0.052 \pm 0.014$ | $-0.021 \pm 0.002$ |
| chopper | $0.084 \pm 0.007$ | $-0.030 \pm 0.003$ |
| horse | $0.102 \pm 0.008$ | $-0.035 \pm 0.004$ |

cats. Accordingly, in Table 3.1, we observe that discrepancy has a similar range for the cat, the elephant and the horse categories and its extrema are closer to 0 for the face category.

Finally, we extend the experimental set with the chopper and the ray shapes. The result is presented in Figure 3.6 (c). First, observe that the chopper shapes are clustered as a separate group in the middle of the other groupings as the chopper category shows both similarities and differences to the other categories. For example, considering the chopper and the face categories, their positive sets are similar (see Table 3.1) but, unlike the face shapes, the chopper shapes have several protrusions. Likewise, considering the chopper and the elephant categories, they are composed of peripheral parts connected to a central body but their parts are not compatible in terms of their number, size and thickness.

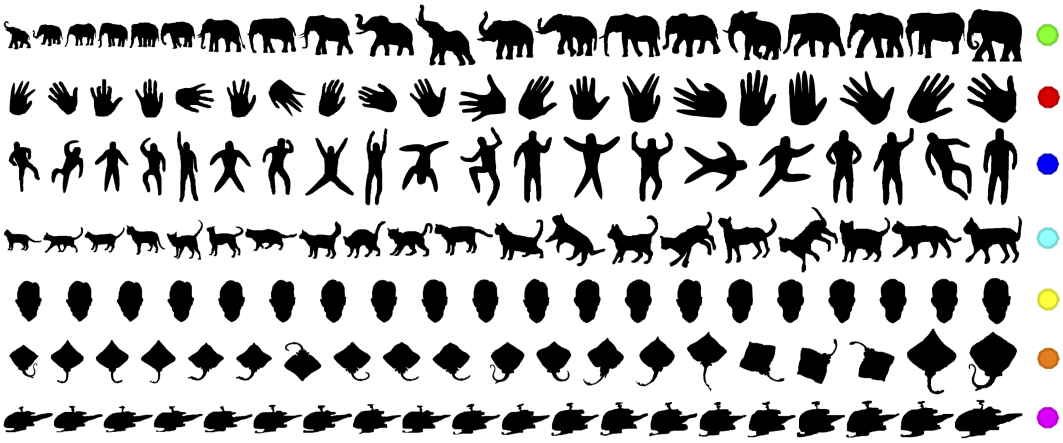

Figure 3.5: Shapes from 7 categories each with 20 instances.

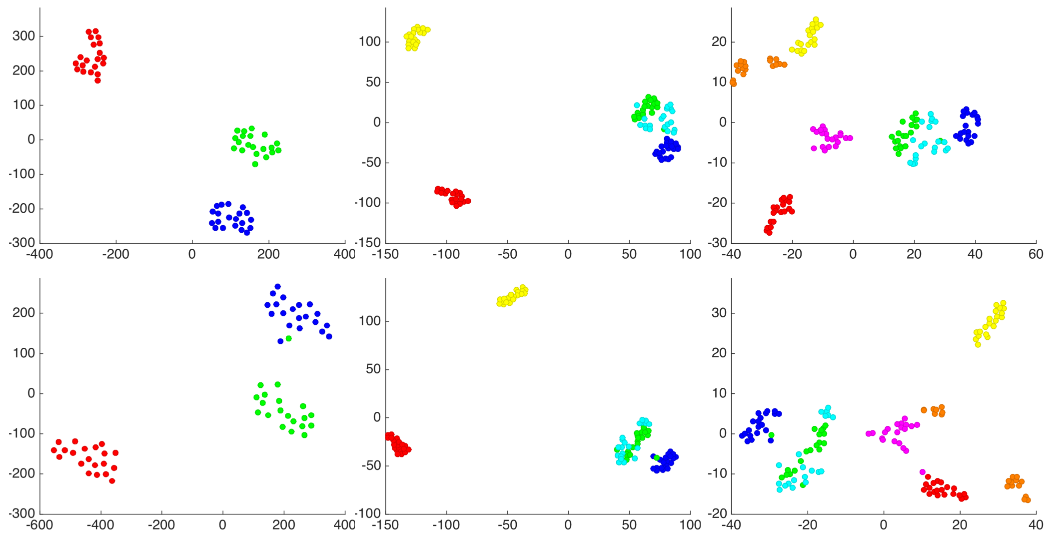

(a) (b) (c)

Figure 3.6: Groupings using discrepancy histogram. (Top) Discrepancy is smoothed with the Gaussian of standard deviation $\sigma = \mathcal{O}(A^{1/2})$. (Bottom) No smoothing is applied. (a) The elephant, the hand and the human shapes. (b) The cat and the face shapes are added. (c) The ray and the chopper shapes are added.

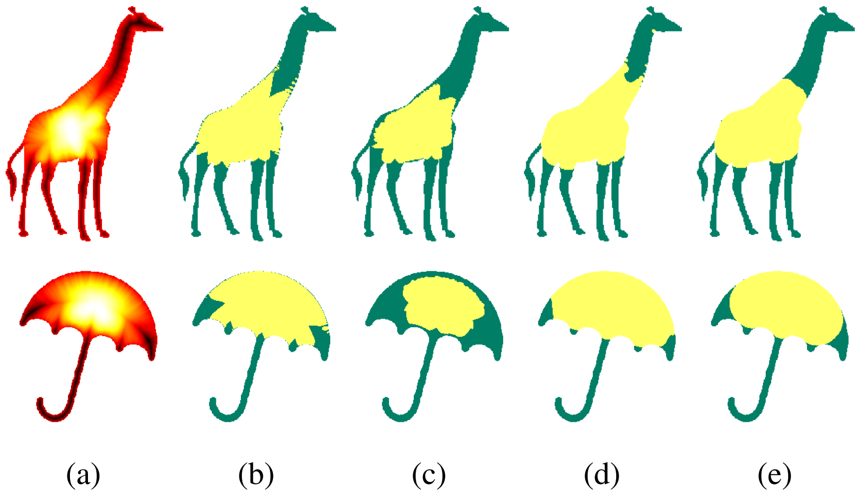

Figure 3.7: (a) Discrepancy. (b) Thresholding at zero. (c) Thresholding at mean value. (d)-(e) Dilating the respective yellow zones.

### 3.3 Application-3: Partitioning

As discrepancy attains positive and negative values where the positives are cumulated on the central region, we may consider splitting the shape domain into two subsets according to discrepancy sign. Another alternative is to use the mean value as a threshold. We have performed partitioning experiments using both alternatives on an extensive shape set and obtained a partitioning result equivalent to those in [38, 39, 18] in a much easier and faster way since one of the functions is calculated via table look up.

In Figure 3.7, partitioning feature of discrepancy is illustrated on two sample shapes. The first one is a giraffe shape with semantically meaningful parts consisting of the body, four legs, tail and head together with neck. The second one is an umbrella shape which can be partitioned into the handle, canopy and four bumps along the canopy edge. We present discrepancy for both shapes in Figure 3.7 (a). By thresholding discrepancy according to its sign, we obtain the partitioning results shown in Figure 3.7 (b) which are consistent with our expectation. When we choose the mean discrepancy value as the threshold, central yellow zones shrink (see Figure 3.7 (c)). In Figure 3.7 (d)-(e), we dilate the respective yellow zones given in Figure 3.7 (b)-(c). In

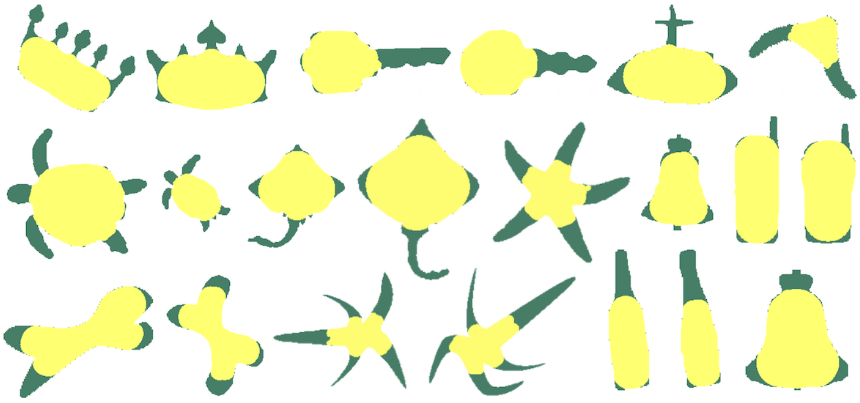

Figure 3.8: Sample partitionings via discrepancy. The mean value is used as threshold. The set composed of larger values is dilated.

this way, the central regions touch the shape boundary and the remaining peripheral regions are further divided (see Figure 3.7 (c) and (e)).

In Figure 3.8, we present sample partitionings via discrepancy. We dilate the set composed of the shape points at which discrepancy is higher than the mean value. Observe how the central regions are captured by the yellow zones and the peripheral parts are obtained via the green sections. Also, we see that the partitioning results are consistent among the shapes from the same category.

In Figure 3.9 (a), we present partitioning of the shape boundary for a set of shapes according to the sign of discrepancy. We smooth discrepancy slightly (see Figure 3.9 (b)) in order to filter the noise resulting from the discretization especially near the shape boundary. Observe that the parts of the shapes corresponding to protrusions, appendages and boundary detail are successfully segmented by simple thresholding as discrepancy does most of the trick. Also, note that the regions surrounded by green contours represent the shape features which are distinctive with respect to the reference shape, a disk with a radius equal to the maximum shape thickness where the thickness at each shape point depends on the distance to the nearest boundary point. First consider the disk shape with regular circular bumps. We see that the boundary detail, the circular bumps, is easily differentiated from the main disk shape. Next consider the four device-2 shapes whose branches are similarly segmented in spite of their variation due to bending, boundary noise and thickness change. Now con-

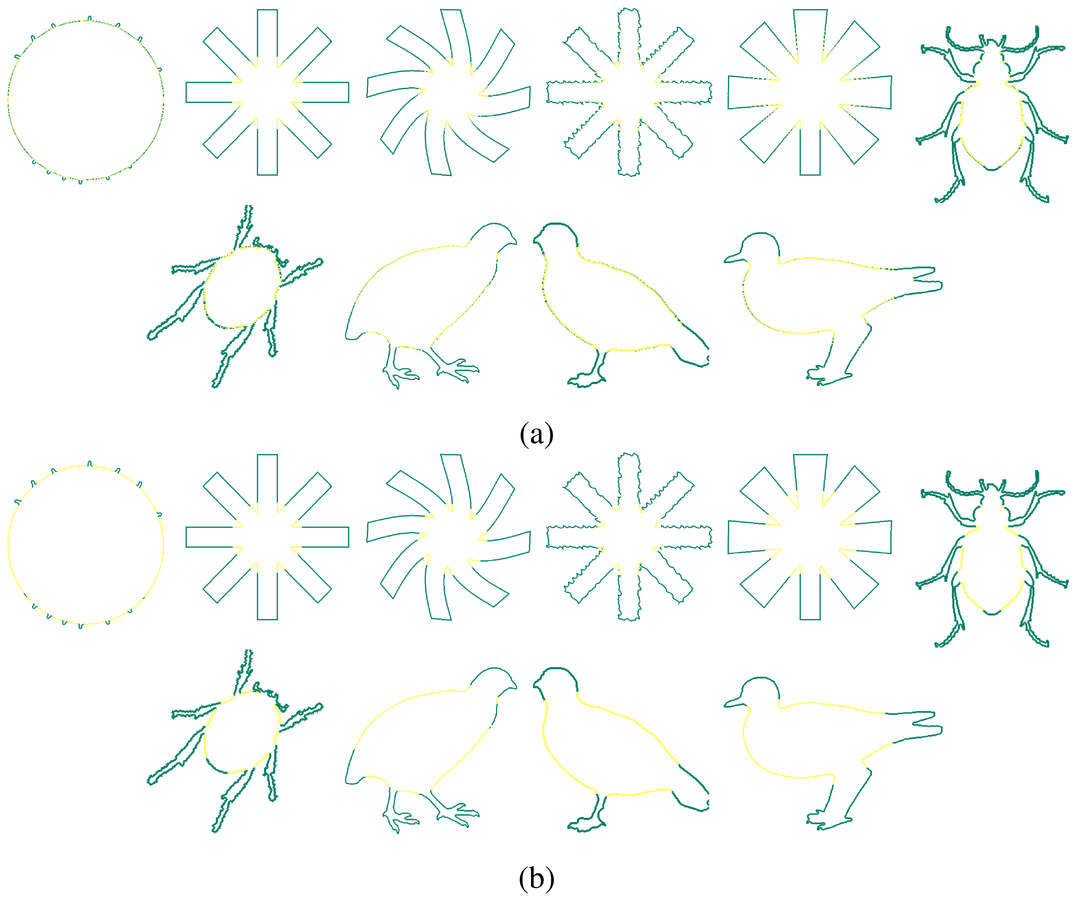

Figure 3.9: Partitioning of the shape boundary for a set of shapes according to the sign of discrepancy. (a) No smoothing. (b) Smoothing with the Gaussian of standard deviation $\sigma = \mathcal{O}(A^{1/4})$.

sider the beetle shapes first of which seems to be more elongated compared to the second one. The head, tail and six legs are separated from the body for both shapes as illustrated by the corresponding green contour fragments. Finally consider the bird shapes which are segmented into the same semantically meaningful parts despite the variation between their bodies in terms of their elongation.

# CHAPTER 4

# A NON-STRUCTURAL REPRESENTATION SCHEME FOR ARTICULATED SHAPES

In this chapter, we present a non-structural shape representation that is robust to transformations such as translation, rotation, scaling and motion of limbs or independent motion of parts called articulations. Our representation involves constructing multiple high-dimensional feature spaces in which the shape points are represented and determining distinctness of the shape points in each space separately via Robust Principal Component Analysis (RPCA). In order to associate each shape point with a high-dimensional feature vector, we solve the PDE (1.6) for varying values of the parameter $a$. Multiple feature spaces are obtained by using different sets of values for the parameter $a$.

The chapter is organized as follows. In § 4.1, we present the motivation behind the proposed representation. In § 4.2, we present our representation scheme and the corresponding shape similarity measure. In § 4.3, we present our clustering results in comparison with the state of the art methods.

## 4.1 Motivation

Articulated shapes can be successfully represented by structural representations which are organized in the form of graphs of shape components such as skeleton (medial axis) fragments. However, it is challenging to build and compare structural representations. For example, in order to obtain a clean and consistent representation, skeleton extraction is frequently assisted by pruning which involves several heuristics. Moreover, measuring similarity of shapes through their structural representations requires finding a correspondence between a pair of graphs, which is an intricate process entailing advanced algorithms.

In this chapter, we present a representation scheme for articulated shapes which involves neither building a graph of shape components nor matching a pair of graphs. The proposed representation is used to measure pairwise shape similarity according to which we cluster a set of shapes. The clustering results obtained on three articulated shape datasets show that our method performs comparable to state of the art methods which utilize component graphs or trees, even though we are not explicitly modeling component relations.

## 4.2 The Method

Our representation scheme relies on first constructing multiple high-dimensional feature spaces in which shape points (pixels in 2D discrete setting) are represented and then, determining distinctness of the shape points in each space separately via RPCA. The distinctness values deduced from each feature space are utilized for two main purposes. First, their spatial distribution on the 2D shape domain is used to partition the shape into a set of regions. Second, each region is described by the normalized probability distribution of the corresponding distinctness values. The dissimilarity between a pair of shapes via each feature space is defined as the cost of the optimal assignment between their regions. Notice that we do not build any graphs to model the shape structure and the optimal assignment problem does not involve matching a pair of graphs. The final shape dissimilarity is computed by combining the dissimilarities deduced from multiple feature spaces.

Below, we present the details of our representation scheme.

### 4.2.1 Construction of a High-dimensional Feature Space

Given a 2D shape, we compute a stack of fields by solving the PDE (1.6) for varying values of the parameter $a$. Each distance field, which is 0 on the boundary and increases towards the center of the shape, is normalized by dividing to its maximum

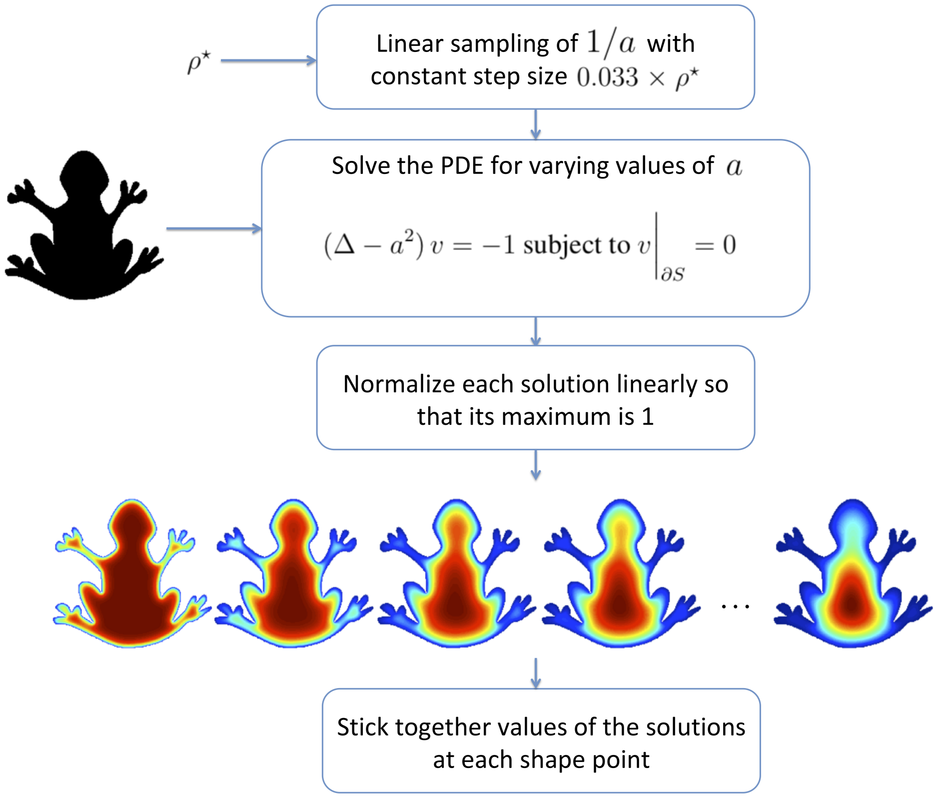


Figure 4.1: Computation of 30-dimensional feature vector at each shape point.

value. We form a feature vector at each shape point by sticking together values of the normalized fields.

By varying $a$, we obtain a collection of features each encoding a different degree of local interaction between the shape points and their surroundings. We vary $1/a$ between $0.033 \times \rho^\star$ and $\rho^\star$ with the constant step size $0.033 \times \rho^\star$, which makes 30-dimensional feature vector at each shape point, where $\rho^\star$ represents the extent of the maximum interaction between the shape points and their surroundings. In order to represent different shapes in a common feature space, we determine $\rho^\star$ for each shape individually as a measurement of the same global shape property.

In Figure 4.1, we summarize the computation of 30-dimensional feature vector at each shape point.

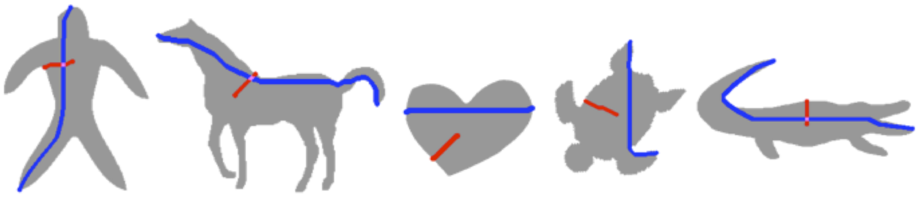

Figure 4.2: $R$ and $G$ correspond to the thickness of the shape body (red) and the maximum distance between the shape extremities (blue), respectively.

### 4.2.2 Determining Multiple High-dimensional Feature Spaces

We utilize two different shape measurements which are related with thickness of the shape body and the maximum distance between the shape extremities. The first measurement $R$ is computed as the maximum value of the shape's distance transform which gives the distance of each shape point from the nearest boundary. The second measurement $G$ is computed as the maximum value of the pairwise geodesic distances between the boundary points where the geodesic distance between a pair of points depends on the shortest path connecting them through the shape domain. As shown in Figure 4.2, $R$ and $G$ provide characteristic shape information which can be used to define the extent of the local interactions between the shape points during the feature space construction. We construct six different feature spaces for which $\rho^\star$ is selected as multiples of $R$ or $G$, namely, $2R$, $3R$, $4R$, $(2/3)G$, $(2/4)G$ and $(2/5)G$.

### 4.2.3 Computing Distinctness of Shape Pixels via Each Feature Space

We organize the feature vectors in the form of a matrix $D \in \mathbb{R}^{m \times 30}$ where each row represents the feature vector computed for a shape pixel and $m$ is the total number of shape pixels. The matrix $D$ is decomposed into a low-rank matrix $L$ and a sparse matrix $S$ via RPCA, which seeks to solve the following convex optimization problem:

$$\min_{L,\, S \,\in \mathbb{R}^{m \times 30}} ||L||_* + \lambda\, ||S||_1 \quad \text{such that} \quad L + S = D \tag{4.1}$$

where $||.||_*$ denotes the sum of the singular values of the matrix, $||.||_1$ is the sum of the absolute values of all matrix entries, and $\lambda$ is the weight of penalizing denseness of the sparse matrix $S$.

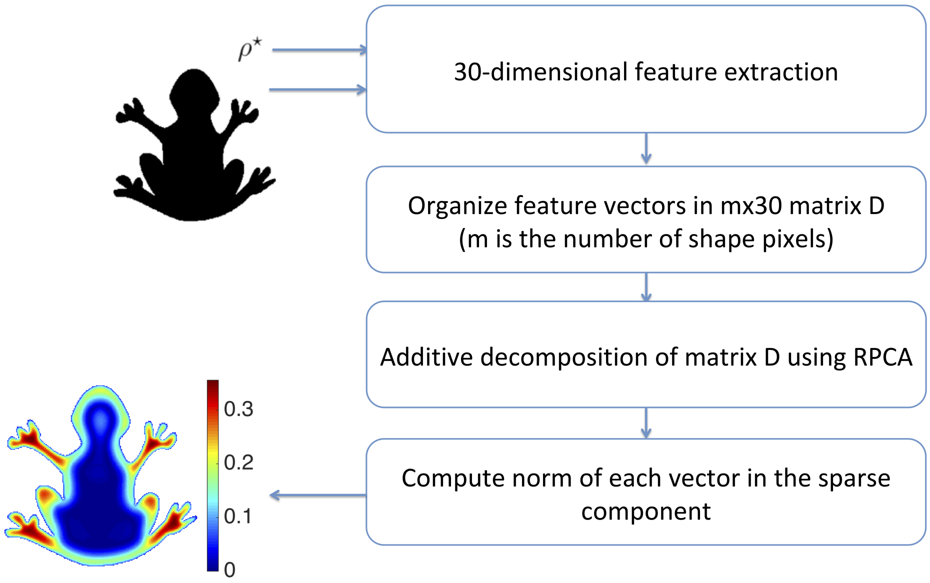


Figure 4.3: Computation of distinctness of the shape pixels.

Various algorithms are proposed to solve the optimization problem in (4.1). We use the inexact augmented Lagrange multipliers method for RPCA [23], which is efficient and highly accurate. We choose $\lambda = 1/\sqrt{m}$ as suggested by the available implementation of [23].

The correlation between the feature vectors hence the shape pixels is encoded by the matrix $L$ whereas their discrimination is contained in the matrix $S$. Thus, we define the distinctness of each shape pixel as the norm of the corresponding vector in the matrix $S$. In Figure 4.3, we summarize computation of the distinctness values.

The shape pixels whose feature components vary more are found to be more distinct. The shape articulations are associated with larger distinctness since they are thinner compared to the shape body and the constant value coming from the shape boundary is propagated faster in these regions during the feature computation.

### 4.2.4 Partitioning Shapes into a Set of Regions via Each Feature Space

We utilize the afore-mentioned property of the distinctness values in order to partition shapes into a set of regions. We first divide the shape domain into two disjoint sets by thresholding at the mean distinctness value. We further partition each set into multiple regions by dilating the two sets one after another in descending distinctness order. In this way, we remove the connections between different regions of each set. Radius of the structuring element used for dilating each pixel is determined using the distance of the pixel from the nearest boundary.

### 4.2.5 Measuring Pairwise Shape Dissimilarity via Each Feature Space

We describe each shape region by the normalized probability distribution of the distinctness values of its constituent pixels where the normalization is performed by making the probability sum equal to the ratio of the region area to the total shape area. In order to estimate the probability distribution, we simply utilize the histogram of the distinctness values with a constant bin size $0.01$. The dissimilarity between a pair of shapes is defined as the cost of the optimal assignment between their regions. We use Hungarian matching for solving the optimal assignment problem. We do not assume any relation between the regions of each shape. Hungarian matching aims to find a one-to-one correspondence between the regions of the two shapes leaving some regions unmatched. The cost of assigning two regions is simply taken as the sum of the absolute value of the difference between their normalized probability distributions. The cost of leaving a region unmatched is taken as the sum of its normalized probability distribution, which is equal to the ratio of its area.

### 4.2.6 Combining Pairwise Shape Dissimilarities Deduced from Multiple Feature Spaces

In order to define the final dissimilarity of a pair of shapes, we compute a weighted average of the dissimilarities deduced from the six feature spaces. The weight is $1/4$ for each of the dissimilarities via the feature spaces constructed using $R$ whereas it is $1/12$ for each of the dissimilarities via the feature spaces constructed using $G$. The non-uniform weighting is due to that $R$ is more reliable than $G$ since the shape body is a more stable structure compared to the articulations.

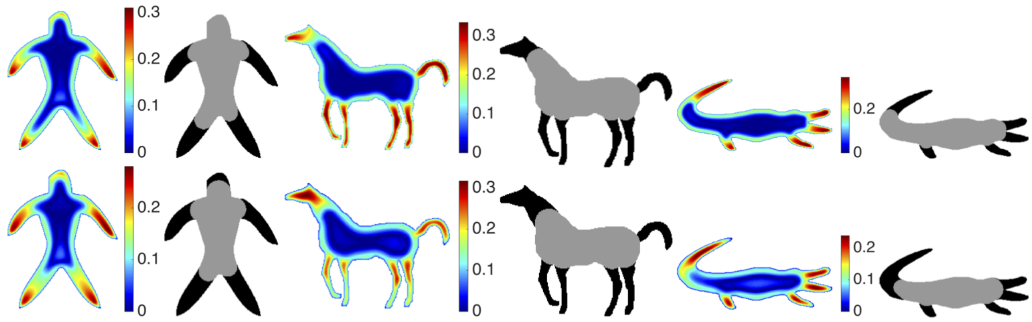


Figure 4.4: Distinctness values (color coded) and the corresponding partitioning results (gray vs. black) for three shapes via the feature spaces constructed for $\rho^\star = 3R$ (top row) and $\rho^\star = (2/4)G$ (bottom row).

## 4.3 Experimental Results

As shown in Figure 4.4, the distribution of distinctness values vary considering representations of different shapes via the same feature space or representations of a single shape via different feature spaces. Grouping of the distinctness values on the shape domain provides partitioning of the shape into meaningful regions such as the shape body (gray) and the articulations (black) via simple operations.

In order to observe the clustering effect implied by the proposed dissimilarity measure, we utilize t-Distributed Stochastic Neighbor Embedding (t-SNE) [41] which aims to map objects into a plane based on their pairwise dissimilarities. In Figure 4.5, we show the t-SNE mapping result for 56shapes [5] dataset which consist of 14 shape categories each with 4 shapes where the within category variations are due to transformations such as rotation, scaling and deformations of articulations. We see that the shapes from the same category cluster together and the shapes from the similar categories (e.g. horse and cat shapes) are close to each other.

We compare our clustering results with state of the art methods using Normalized Mutual Information (NMI). NMI measures the degree of agreement between the ground-truth category partition and the obtained clustering partition by utilizing the entropy measure.

Let $n_i^j$ denote the number of shapes in cluster $i$ and category $j$, $n_i$ denote the number

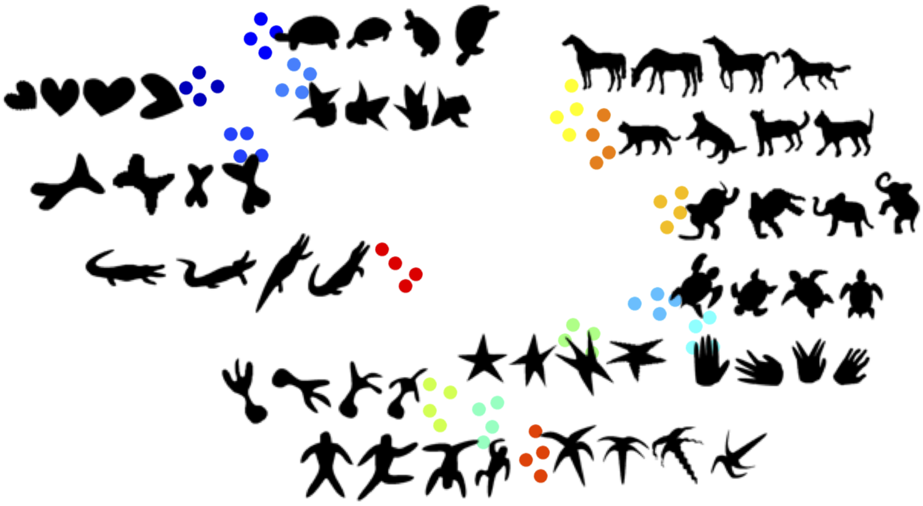

Figure 4.5: t-SNE mapping of the shapes from 56shapes dataset using the proposed dissimilarity measure.

of shapes in cluster $i$, and $n^j$ denote the number of shapes in category $j$. Then NMI can be computed as follows:

$$\frac{2\sum_{i=1}^{I}\sum_{j=1}^{J}\left(n_i^j/N\right)\log\left(\frac{\left(n_i^j/N\right)}{\left(n_i/N\right)\left(n^j/N\right)}\right)}{-\sum_{i=1}^{I}\left(n_i/N\right)\log\left(n_i/N\right)-\sum_{j=1}^{J}\left(n^j/N\right)\log\left(n^j/N\right)} \tag{4.2}$$

where $I$ is the number of clusters, $J$ is the number of categories and $N$ is the total number of shapes.

A high value of NMI indicates that the obtained clustering matches well with the ground-truth category partition. In order to compute NMI of our clustering result, we need to assign a cluster id to each shape. Given the t-SNE mapping of a dataset obtained using our proposed dissimilarity measure, we apply affinity propagation [15] to partition the dataset into a number of clusters (which is chosen equal to the number of categories in the dataset).

In Table 4.1, we present NMIs of our proposed method and other state of the art methods on 56shapes [5], 180shapes [4] and 1000shapes [10] datasets. 180shapes dataset consist of 30 categories each with 6 shapes. 1000shapes dataset consist of 50 categories each with 20 shapes. CSD [35] employs hierarchical clustering in which a common shape structure is constructed each time two clusters are merged into a single cluster where building a common shape structure requires matching skeleton graphs.

Table 4.1: The clustering performance comparison using NMI.

| | 56shapes | 180shapes | 1000shapes | Average |
|---|---|---|---|---|
| CSD | 0.9734 | 0.9694 | 0.8096 | 0.9175 |
| IDSC+Ncuts | 0.5660 | 0.5423 | 0.5433 | 0.5505 |
| Shape context+spectral | 0.9418 | 0.9264 | **0.9676** | 0.9453 |
| Skeleton path+spectral | 0.9426 | **0.9746** | 0.9154 | 0.9442 |
| Proposed method | **1.0000** | 0.9651 | 0.9177 | **0.9609** |

The method (skeleton path+spectral) presented in the work [8] combines the skeleton path distance [9] with spectral clustering. The performance of these two skeleton-based methods decreases for 1000shapes dataset which contains unarticulated shape categories such as face category. For 1000shapes dataset, the highest performance is obtained via the method (shape context+spectral) in [8] which uses shape context descriptor [11]. As the shape context descriptor is not robust to deformation of shape articulations, the performance decreases for highly articulated 56shapes and 180shapes datasets. Inner distance shape context (IDSC) descriptor [24] is an articulation invariant alternative to the shape context descriptor. In the work [35], the performance of IDSC combined with normalized cuts algorithm is reported for the three datasets. Overall, we accurately cluster the shapes from 56shapes dataset and our proposed method has the highest NMI average over the three datasets. We observe that without constructing and matching graphs of shape components, our method performs comparable to the structural methods.

# CHAPTER 5

# A NON-LOCAL MEASURE FOR MESH SALIENCY

In this chapter, we present a non-local measure of saliency defined on the surface of a 3D shape represented as a mesh. The framework that we follow is similar to the one presented in the previous chapter. We represent the mesh points in a high-dimensional feature space and determine their discrimination by applying Robust Principal Component Analysis (RPCA). However, instead of utilizing the PDE (1.6) for varying values of the parameter $a$, we construct a high-dimensional feature space by solving the PDE (1.8) for varying right hand side functions $f$ where $a$ is fixed to a sufficiently small value.

The chapter is organized as follows. In § 5.1, we present the motivation behind the mesh saliency measure. In § 5.2, we present the method for computing it. In § 5.3, we give illustrative results obtained via the proposed saliency measure.

## 5.1 Motivation

A perception scientist, Attneave, observed that the set of points that best represent a shape is taken from the regions where the bounding contour is most different from a straight line [6]. Furthermore, using random shapes created by linking points, he found a linear relationship between judged complexity and the logarithm of the number of points [7]. This link has been exploited by many computational methods addressing a variety of tasks including contour partitioning. Later studies such as [43] also confirmed Attneave's hypothesis [6] that curvature extrema are salient points, but while also showing that the perceptual saliency of a point along the contour is determined by more factors than just local absolute curvature and the contour perception

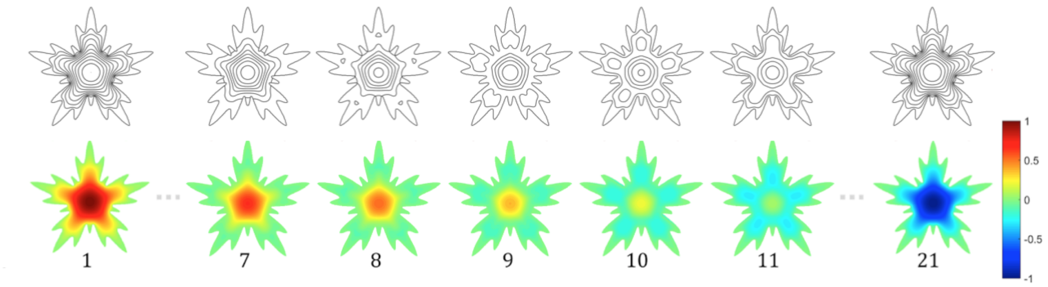


Figure 5.1: For illustration purposes, we used a planar domain consisting of pixels and showed a sequence of feature values at each pixel. At the top row, level curves of the fields composed of the feature values are presented.

is strongly influenced by non-local factors.

In this chapter, we present a saliency measure (in the form of one-parameter family of functions defined over the shape surface) that depend on both local and non-local factors. Instead of contours that bound regions, we focus on surfaces that bound volumes. As compared to classical computational problems of saliency of positions in images or contours, with numerous computational realizations over the course of nearly six decades, saliency of positions on a bounding surface is relatively less explored.

### 5.2 The Method

The method consists of forming a high dimensional representation, and then reducing it via RPCA. Local to global integration is achieved gradually in two steps. First, during the construction of the high dimensional feature space (§ 5.2.1). Second, during low dimensional reduction (§ 5.2.2).

We assume the data is a set of voxels on a regular grid, forming the interior of a domain in the three-dimensional space.

#### 5.2.1 Feature Space

Using a domain labelling formulation from our recent work on hierarchical domain decomposition [18], we construct multiple labels $\in [-1, 1]$ for each interior voxel of a given domain. In Figure 5.1, for illustration purpose, sample labels on a 2D planar domain are depicted. The labels assigned to the pixels at each step of the sequence form a smooth field over the shape domain. At the top row, level curves of the fields are presented. At the first/last step, the labels are composed of positive/negative values, respectively. At the intermediate steps, the labels are negative on the shape periphery and positive on the central shape region. Level curves of the fields provide hierarchical partitioning of the shape domain. The goal of the original work in [18] is to find the right selection of label assignments that yields proper hierarchical partitioning of the domain. Hence, eventually one specific setting is selected while all the other are discarded. In the case of Figure 5.1, that is somewhere between the eighth and ninth. In contrast, in the presented work, all possible label assignments are kept so that each voxel is characterized by multiple label values. Since our interest is on the mesh of the bounding surface, a value transfer from the interior voxels is required. This is done by assigning each boundary mesh element the value of the nearest interior voxel.

Before giving the details of the labelling process and arguing why it is appropriate in the present setting, let us demonstrate the coding capability of the suggested feature. For demonstration, we select 16 sample points with differing local and global characteristics on the armadillo surface (see Figure 5.2 (left)). These include points representing regions of various local curvature and volumetric thickness, distributed over the surface to characterize the global structure. At each sample point, we compute 21 label values and divide them to their maximum absolute value so that their range is fixed to $[-1, 1]$. As the sample points can be differentiated according to how the corresponding labels change in the range $[-1, 1]$, the piecewise linear curve formed by linking the consecutive labels is called as the signature of the sample points. In the following three paragraphs, we discuss that the 21-dimensional feature values are capable of differentiating local and global characteristics of the boundary surface.

Firstly, features at regions with locally small thickness (including curvature maxima) such as ears, fingers, nose and tail (red points) exhibit sharp decay in the early stages of the signature, whereas we observe smoother decay at regions with locally larger thickness such as the torso.

Secondly, the effect of global structure is observed comparing signatures of the points

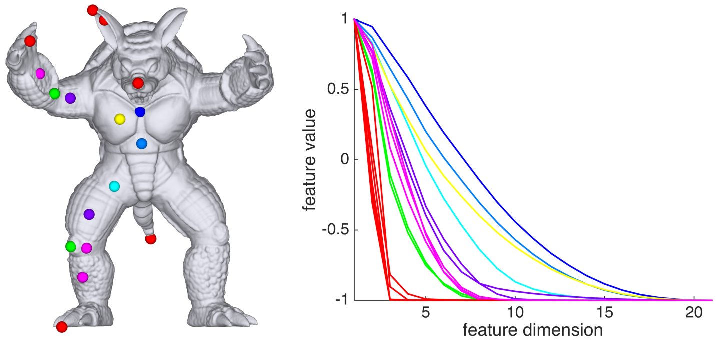


Figure 5.2: For various points on armadillo surface, plots of feature vectors at selected locations on the mesh. The correspondence between the points and their plots is color coded.

selected over the surface of the arm and leg. Notice how structurally corresponding points on these parts (purple, green, pink and red points) have similar signatures reflecting their relative proximity to the shape center (torso), despite the fact that local thickness of the forearm is larger than the upper arm in contrast to the thickness configuration observed in the parts of the leg.

Thirdly, the pink and green points within the proximity of the left knee exemplify how the feature finds the balance in encoding the local and global characteristics. We note that the green point is located on the knee cap which slightly protrudes from the leg whereas the pink point represents a smooth part of the knee. The feature successfully distinguishes these points with different local characteristics despite their similar position with respect to the global structure.

The intuitive idea of the labelling process is to construct a field inside the volume such that its value at a voxel depends on both long range and short range interactions among domain elements, *i.e.* voxels. For computational convenience and ease of implementation, the following three-step procedure is used. At the first step, each voxel is assigned its distance to the nearest boundary point. This gives the classical distance transform, which codes long range interactions among opposing boundary elements. The second step is a thresholding step, which makes a hypothetical central peripheral split of the domain. At this step, after the distances are normalized to $(0, 1]$ range, voxels whose normalized distances are smaller than a control parameter

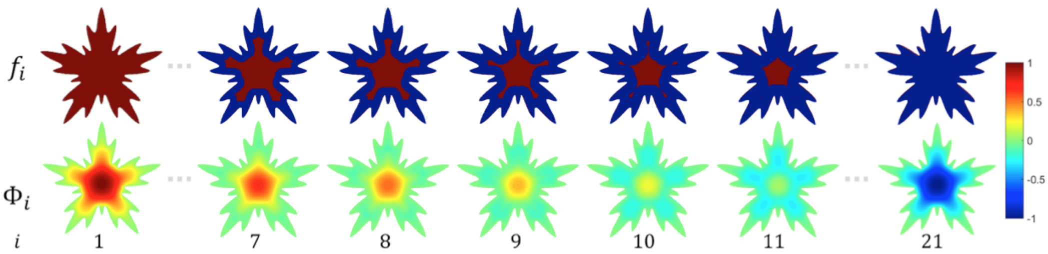


Figure 5.3: The initial binary labels (top row) are relaxed via local averaging to obtain the final labels (bottom row).

$\in [0, 1]$ are assigned $-1$, whereas the others are assigned $+1$. The set of values used for the control parameter is determined by sampling the range $[0, 1]$ with the constant step size $0.05$, which makes 21 different threshold values.

Initial binary labels are depicted in Figure 5.3 top row where the control parameter increases from left to right and the binary labels $-1$ and $+1$ are shown using dark-blue and dark-red colors, respectively. The positive voxel set is a kind of soft barrier for the contour information. It can be thought as an indirect way of changing the speed of final relaxation. At each level $i$, the final labels $\Phi_i$ are obtained from the initial labels $f_i$ via the PDE $(\Delta - 1/|\Omega|^2)\,\Phi_i = -f_i$ subject to $\Phi_i = 0$ on the shape boundary $\partial\Omega$ where $|\Omega|$ corresponds to the number of nodes in the shape domain $\Omega$. Notice that this PDE is the same PDE in (1.8) when $a = 1/|\Omega|$. As can be deduced from the associated energy (1.7), the finals labels $\Phi_i$ represent smoothed form of the initial labels $f_i$. We normalize each $\Phi_i$ by dividing its values to the maximum absolute value of all $\Phi_i$. Note that as the control parameter approaches to 0 or 1, the positive or the negative set covers the entire domain, hence, no barrier effect is introduced during the relaxation step.

The relevant point is that the final labels are the result of mixed complex interactions among domain elements, whether long range or short range. Furthermore, each case reflects a particular bias on the partitioning structure as indicated during the thresholding step where a control parameter bounded by the domain thickness is defined. The control parameter determines the effect of non-locality. The labels are defined for interior voxels where the value on the boundary is fixed at 0. Hence, a value transfer is performed by assigning each boundary mesh element the label of the nearest interior voxel.

Next step is to re-organize this high dimensional information represented via labels in a way to yield a local to global measure of saliency as detailed in § 5.2.2. Eventually, our goal is to distinguish the surface points that represent observations that are less frequent, and as such considered salient with respect to the global configuration.

### 5.2.2 Reduction via Robust Principal Component Analysis

The process starts with forming a matrix $D \in \mathbb{R}^{m\times 21}$ of which columns denote the feature values at each of $m$ mesh locations. This is followed by an additive decomposition of $D$ into a low-rank matrix $L \in \mathbb{R}^{m\times 21}$ and a sparse matrix $S \in \mathbb{R}^{m\times 21}$ via RPCA where the sparseness of $S$ is determined by the parameter $\lambda$. See § 4.2.3 for RPCA details.

The low rank component $L$ is expected to encode correlations among the mesh points via their feature values whereas the sparse component $S$ is expected to encode their discriminations as it contains the residuals stemming from less frequent feature configurations.

In order to assess the saliency of a mesh element, we simply compute the norm of the corresponding row vector in the matrix $S$.

By varying the sparseness parameter $\lambda$, we obtain different measures of saliency at each location.

## 5.3 Results and Discussion

In the experiments, as a proof of concept, we find it sufficient to divide the possible range (the domain width) to 20 equal intervals, hence compute 21 possible label assignments. This number can be increased or made to reflect the domain size.

In Figure 5.4, we present saliency results obtained for armadillo model for increasing values of the parameter $\lambda$ ($= 1/m$, $1/m^{0.625}$ and $1/m^{0.5}$). Salient regions are depicted with red tones whereas blue tones indicate non-salient regions.

Figure 5.4: Saliency results obtained for armadillo model using $\lambda = 1/m$, $\lambda = 1/m^{0.625}$ and $\lambda = 1/m^{0.5}$, respectively, where $m$ is the number of surface points. Salient regions are depicted with red tones whereas blue tones indicate non-salient regions.

The parameter $\lambda$ adjusts the sparseness of the matrix $S$ and hence affects the localization of the salient regions in the input surface. As the sparsity increases, salient points on the surface gets more and more localized and almost come to an agreement with the local curvature maxima.

For a small value of $\lambda$ ($= 1/m$), we obtain a denser matrix $S$ emphasizing the saliency of the global structures, i.e. shape parts. As illustrated in Figure 5.4 (left), the arms, legs, ears, tail and mouth of armadillo are found as salient.

For the larger values of $\lambda$ ($= 1/m^{0.625}$ and $1/m^{0.5}$), we observe that salient regions become gradually more localized. Consider Figure 5.4 (right) with the saliency result for the largest chosen $\lambda$ ($= 1/m^{0.5}$). We obtain a saliency measure which captures the local curvature maxima of armadillo model such as the finger tips, the nose, the edges of the ears and the tail tip.

Selecting $\lambda$ between the smallest and the largest chosen value produces more than in-between results. For example, regions that are close to the central blob are emphasized (see the chest of armadillo in Figure 5.4 (middle)).

More illustrative saliency results are presented in Figure 5.5. For the smallest chosen $\lambda$, shape parts are found as salient such as the head, legs and tail of the horse, the legs and antennas of the ant, the wings and nose of the airplane, the smaller one of the merged cubes and the hollowed front part of the larger cube, the fingers of the hand

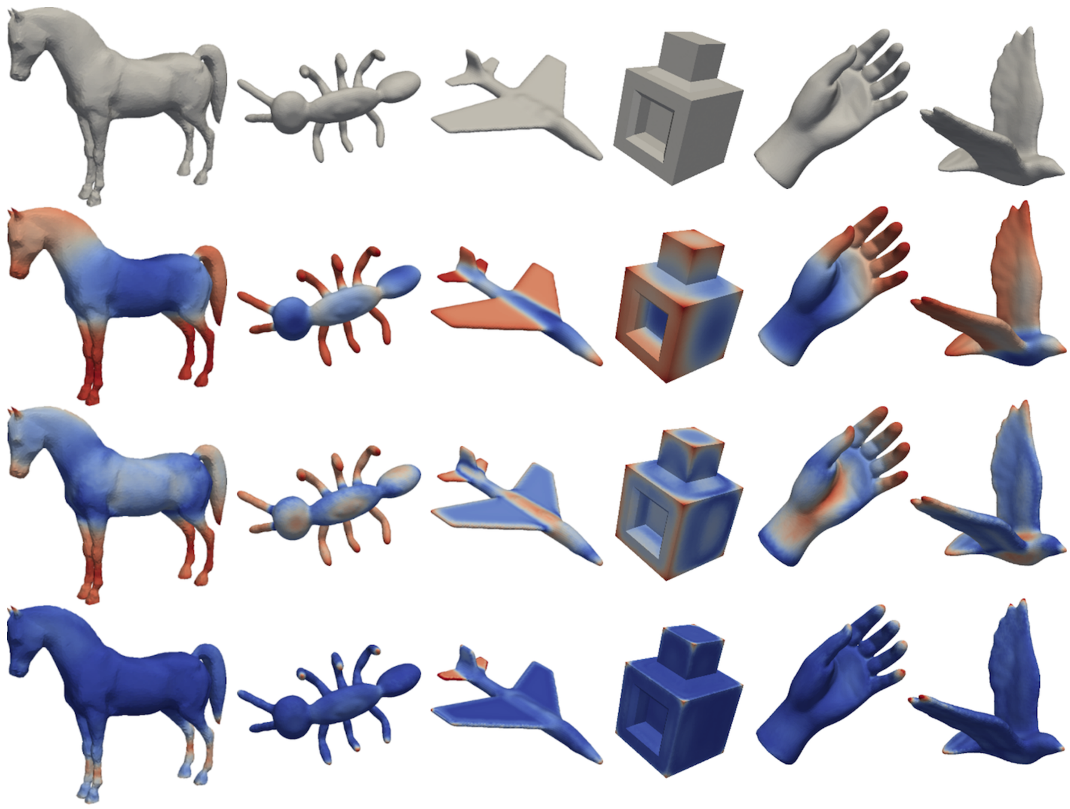

Figure 5.5: Input surfaces are shown in the first row, and saliency results obtained using $\lambda = 1/m$, $\lambda = 1/m^{0.625}$ and $\lambda = 1/m^{0.5}$ are presented in the remaining rows, respectively. Warmer colors represent salient regions.

and, lastly, the wings, nose and tail of the bird (see the second row in Figure 5.5). For the largest chosen $\lambda$, the local curvature maxima (such as the tips of the protrusions and the corners of the cubes) and the thinnest structures (such as the bottom part of the horse legs and the rear wings of the airplane) are emphasized (see the fourth row in Figure 5.5). When $\lambda$ is between the smallest and the largest chosen value, regions close to central blobs are found as salient such as the palm of the hand and the body of the bird (see the third row in Figure 5.5).

Figure 5.6: Saliency result obtained for the armadillo model via the method in [22]. Warmer colors represent salient regions.

In Figure 5.6, we present the saliency result obtained for the armadillo model via the method in [22] which measures the difference of regions from their surroundings with respect to their mean curvature. As it is computed via the difference of a local feature in a local neighborhood, the obtained saliency measure is a local one emphasizing curvature extrema.

### 5.3.1 Grouping Mesh Vertices Using Multiple Saliency Measures

We obtain multiple saliency measures by varying $\lambda$ parameter of RPCA. For observing grouping of mesh vertices via these multiple measures, we first construct $m \times m$ distance matrix where pairwise distance of the vertices is computed as Euclidean distance between their saliency values. We utilize rows of the distance matrix as $m$-dimensional feature vectors representing $m$ mesh vertices. We then apply dimensionality reduction, specifically t-SNE, for mapping each vertex to a single value. t-SNE maps similar features to nearby points and dissimilar features to far away points and hence the values obtained via t-SNE provide grouping of the mesh vertices. In Figure 5.7, we present the values assigned to the surface points of the armadillo model via t-SNE mapping using the three saliency measures shown in Figure 5.4. We see that regions of the surface associated with a similar saliency over different choices of $\lambda$ parameter are grouped together. Notice that how regions with a small bump such as knees and breasts are differentiated from their surroundings.

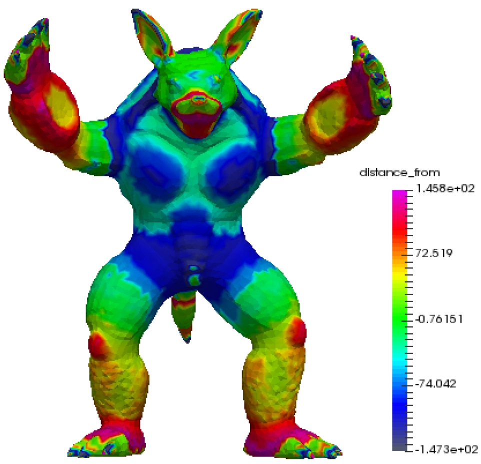


Figure 5.7: Grouping of mesh vertices using the multiple saliency measures shown in Figure 5.4.

# CHAPTER 6

# EQUATING SHAPE TOPOLOGIES UNDER TOPOLOGICAL NOISE

In this chapter, we present a method that brings a pair of 3D shapes into comparable topology via their adaptive deflation. The deflations are controlled by a pair of transformations defined in the whole shape domain. The first transformation whose iso-surfaces provide shape simplifying deflations is the minimizer of the energy (1.7) where $f$ is selected as the Euclidean Distance Transform (EDT) of the shape and $a$ is chosen as a sufficiently small value. The second transformation providing a central structure for stopping deflations is obtained as the minimizer of a modification of the same energy (1.7).

The chapter is organized as follows. In § 6.1, we present the motivation and related work for handling topological differences between 3D shapes. In § 6.2, we present our topology equating strategy. In § 6.3-6.4, we present the experimental results.

## 6.1 Motivation and Related Work

Advancement of visual data acquisition technology enabled easy acquisition of 3D shapes in the form of surface meshes enclosing solid objects. These meshes are used in many computer vision and graphics applications, many of which require establishing meaningful correspondences that pair up semantically equivalent points on two surfaces. The process of pairing up is called *matching*. For a matching result to be of practical value, the matched points should be semantically equivalent where the semantic equivalence needs to be inferred from the geometrical and topological properties. Typically, however, geometrical and topological information is corrupted by noise, which may get added either during acquisition or model formation.

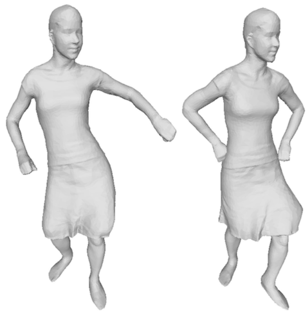

Figure 6.1: A pair of 3D shapes from MIT samba sequence [42]. Model on the right has hands connected to the belly.

The methods that address the problem of matching under topological noise can be classified into two groups: model-based and model-free. The techniques in the first group require a prior shape model. The topological complications are resolved by aligning the prior model with each one of the shapes [42]. A disadvantage of model-based techniques is that they require good prior models which may not always be available. In such situations, a model-free approach may be the only option.

One model-free technique is to register a pair of 3D shapes via their spectral embedding, after eigenvector re-ordering [26]. Despite the effort spent on re-ordering, the matching is tolerant only to moderate noise. The most common strategy in model-free techniques is to replace topology-sensitive distances with robust ones [33, 14, 1, 34, 29]. Note that a measure of dissimilarity (distance) is required if one wants to find the similar pairs. The usual distance is the geodesic distance (which depends on the shortest path between a pair of points). Naturally, the choice of the distance affects the quality of the matching. For example, the geodesic distance is robust only to certain class of deformations, yet sensitive to topological changes. Diffusion based distances corresponding to an average of all the paths between the pair of points are less sensitive, hence, commonly employed in the literature [33, 14, 1, 34, 29]. The diffusion distances, however, are sensitive to the choice of the scope of averaging, *i.e.* the scale parameter. Therefore, in some works [34, 29], diffusion distances at multiple scales are employed to achieve robustness to topological changes.

In this chapter, we focus on a particular type of topological noise: One that is unavoidable even if the physical capabilities of the acquisition system is of very high quality, e.g. an arm touching the body during a motion capture session (Figure 6.1). Our approach is to adaptively deflate the pair of shapes for the purpose of bringing the pair of shapes to be matched to a comparable topology before the search for the correspondences. Once the pair of shapes is brought to a topologically comparable form, the matching is performed between topologically comparable forms and then the found correspondences are transferred to the correspondences between the original pair of input shapes. Previously, Genctav et al. [16] inflated and deflated surface meshes with the help of a smooth indicator function proposed in Tari et al. [40]. In this chapter, we present a new and more systematic topology equating process by employing two volumetric transformations, each of which is an approximation of the EDT subject to competing regularities. This pair of transformations enables us to implement the deflation process more systematically, to robustly handle scale normalization, and to define a stopping condition. We denote the transformations by $\rho^0$ and $\rho^1$ where the superscripts $0$ and $1$ indicate the values of a binary parameter used in their computation via a common model presented in the next section.

## 6.2 Adaptive Deflations via $\rho^0$ and $\rho^1$

The transformation $\rho^0$ is merely a smooth approximation of the EDT. It facilitates the generation of a collection of iso-surfaces that represent adaptive shape simplifying deflations of the shape boundary parameterized by a deflation level $\ell \in [0, 1]$; the larger the $\ell$ the more is the deflation hence the simplification. The deflations are adaptive: At any fixed level $\ell \in [0, 1]$, the amount of deflation at a point $\mathrm{p}$ of the deflating surface depends on the surface features that are implicitly coded through the values of $\rho^0$ in an $\epsilon-$neighborhood of $\mathrm{p}$. We discretize $\ell$ by sampling its range $[0, 1]$ at a fixed length $\delta = 0.004$.

Deflations are merely selected iso-surfaces of $\rho^0$. In order to make sure that the process of deflating stops at an appropriate level so that the set of deflations is of practical value, *i.e.*, the process does not yield trivial surfaces for any $\ell \in [0, 1]$, we construct a *barrier structure*. The barrier structure is used to automatically stop topology equating adaptive deflations. The details of the construction process which makes use of $\rho^1$ and the EDT will be given in a later subsection.

Once we have a collection of iso-surfaces for each of the shapes, we follow the same steps as in Genctav et al. [16] in order to choose the pair of iso-surfaces that is to be considered as topologically comparable forms of the input shapes. First, we determine the levels at which the iso-surfaces from both shapes have comparable topology. We quantify topology of the iso-surfaces in terms of their genus number that intuitively counts the number of handles of a given object. In order to compute genus number of the iso-surfaces, we employ the Euler formula which is applicable to closed and connected manifold meshes. Suitably, the extracted iso-surfaces are always composed of closed meshes since the corresponding transformation $\rho^0$ is smooth and continuous. However, the iso-surfaces can have more than one mesh component and each component may contain non-manifold vertices or edges. Thus, we consider the largest mesh component in terms of vertex count and apply the Euler formula after checking its manifoldness. Second, we take the smallest one among the genus numbers shared between pairs of iso-surfaces. The iso-surfaces are more similar to input shapes at preceding levels so we choose the first pair of iso-surfaces corresponding to the selected genus as the topologically comparable forms of the input shapes.

### 6.2.1 Computing $\rho^\beta$

We now explain how $\rho^0$ and $\rho^1$ are computed via a common formulation. Let $\Omega \subset \mathbb{R}^3$ denote the volume enclosed by the surface mesh of the shape. Further let $\partial\Omega$ denote the boundary of $\Omega$. The two regularized approximations to the EDT, namely $\rho^0$ and $\rho^1$, are obtained as the minimizers of the energy given in (6.1), where the binary valued parameter $\beta \in \{0,\ 1\}$ is set to $0$ and $1$, respectively.

$$
\begin{aligned}
&\arg\min_{\rho^\beta} \int_\Omega \big(E_d(\rho^\beta) + E_s(\rho^\beta) + \beta E_a(\rho^\beta)\big)\,\mathrm{d}\omega \text{ subject to } \rho^\beta = 0 \text{ on } \partial\Omega \\
&\qquad E_d(\rho^\beta) = \frac{1}{O(|\Omega|)}\left(\rho^\beta - EDT^\Omega\right)^2 \\
&\qquad E_s(\rho^\beta) = \left|\nabla \rho^\beta\right|^2 \\
&\qquad E_a(\rho^\beta) = \frac{1}{O(|\Omega|)}\Big(\int_\Omega \rho^\beta\,\mathrm{d}\omega\Big)^2
\end{aligned}
\tag{6.1}
$$

Observe that $E_d$ decreases as $\rho^\beta$ gets closer to the EDT, $E_s$ decreases as $\rho^\beta$ becomes smoother and $E_a$ decreases as the global average of $\rho^\beta$ approaches $0$. Notice that the energy associated with $\rho^0$ is the same as (1.7) where $f = EDT^\Omega$ and $a = 1/O(|\Omega|)$.

The difference between the volumetric transformation $\rho^0$ and the smooth distance function used in the preliminary work [16] is the following. $\rho^0$ minimizes the energy (1.7) whereas the former one minimizes the energy (1.2). Roughly speaking, $\rho^0$ is a smoothing of the EDT whereas the former one is a smoothing of the characteristic function which is 1 on the shape and 0 elsewhere. This minor distinction is indeed important in terms of obtaining a simplified adaptive level separation. In the following subsections, we show that the topology equating process takes less number of steps when we use $\rho^0$ to extract shape deflations.

The second volumetric transformation, $\rho^1$, is based on the 2D region segmentation field model from [38, 37]. $\rho^1$ is a smooth function that takes both positive and negative values so that the absolute value of its global average is minimized. $\rho^1$ is positive at the inner shape regions where the EDT is high, whereas it is negative at the outer shape regions where the EDT is low. The zero-crossing of $\rho^1$ provides a partitioning of the shape into central and the remaining outer regions. In our work, we utilize $\rho^1$ to perform the scale normalization between the input pair of shapes as well as to extract a suitable stopping condition via what we refer as the barrier structure.

### 6.2.2 Barrier Structure

The volumetric transformation $\rho^1$ has two phases – negative (outside) and positive (inside). The phase boundary given by the zero-crossing of $\rho^1$ separates the entire volume (enclosed by a surface) into two disjoint sets, one of which captures the central structure as illustrated in Figure 6.2 (a). We dilate this central structure so that it touches the shape boundary and obtain the barrier structure, a coarse shape without appendages (see Figure 6.2 (b)). In order to extract the iso-surface that represents the maximum deflation allowed (the iso-surface at $\ell = 1$), we use $\rho^0_\star$ which is the maximum value of $\rho^0$ inside the shape volume and outside the barrier structure. Accordingly, the iso-surface at an intermediate level $\ell$ is extracted using the value $\ell \times \rho^0_\star$. In this way, we consider meaningful deflations preserving the essential shape struc-

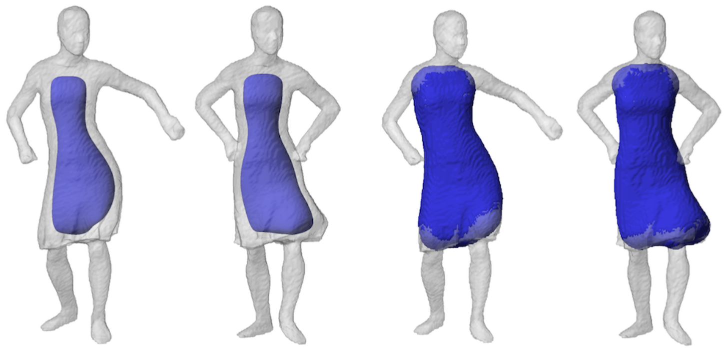

(a) (b)

Figure 6.2: (a) Central structures (b) Barrier structures for the shapes in Figure 6.1.

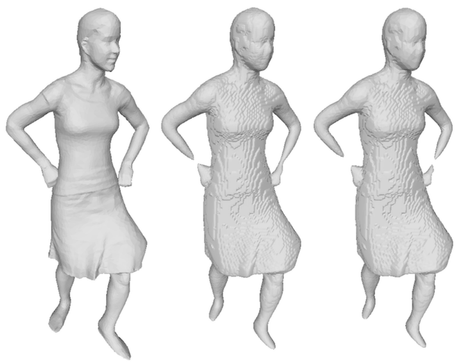

Figure 6.3: The second shape in Figure 6.1 and iso-surfaces of the corresponding $\rho^0$ at $\ell = 0.044$ and $\ell = 0.052$.

ture. Notice that the deflations cannot fully enclose the barrier structure since the deflations are inside the shape boundary whereas the barrier structure touches the boundary. Instead of stopping the deflations according to their intersection with the barrier structure which needs to be computed for each of them, we simply consider the iso-surface of $\rho^0$ with the value $\rho^0_\star$ as the maximum deflation.

### 6.2.3 An Illustration

In Figure 6.3, we present a shape from MIT samba sequence [42] (which is the second shape in Figure 6.1) along with the iso-surfaces of the corresponding $\rho^0$ at $\ell = 0.044$ and $\ell = 0.052$. Note that hands of the shape are touching the belly and the wrists disappear first in the deflated forms of the shape boundary because they are the thinnest parts of the shape. At $\ell = 0.052$, both of the arms are separated from the belly while the essential shape structure is preserved.

In Table 6.1, we present summary of the notions used throughout the text. In Figure 6.4, we illustrate the topology equating process.

Table 6.1: Summary of the notions used throughout the text.

| | |
|---|---|
| Shape volume | $\Omega' \subset R^3$ |
| Negative phase | $\{x \,|\, x \in \Omega'$ and $\rho^1(x) < 0\}$ |
| Positive phase | $\{x \,|\, x \in \Omega'$ and $\rho^1(x) > 0\}$ |
| Zero-crossing (Phase boundary) | $\{x \,|\, x \in \Omega'$ and $\rho^1(x) = 0\}$ |
| Barrier structure | Dilation of the positive phase so that it touches the shape boundary |
| $\rho^0_\star$ | $\max(\{\rho^0(x) \,|\, x \in \Omega'$ and $x \notin$ Barrier structure$\})$ |
| Deflation at level $\ell$ where $\ell \in [0, 1]$ | $\{x \,|\, x \in \Omega'$ and $\rho^0(x) = \ell \times \rho^0_\star\}$ |
| Maximum deflation | Deflation at level $\ell = 1$ |

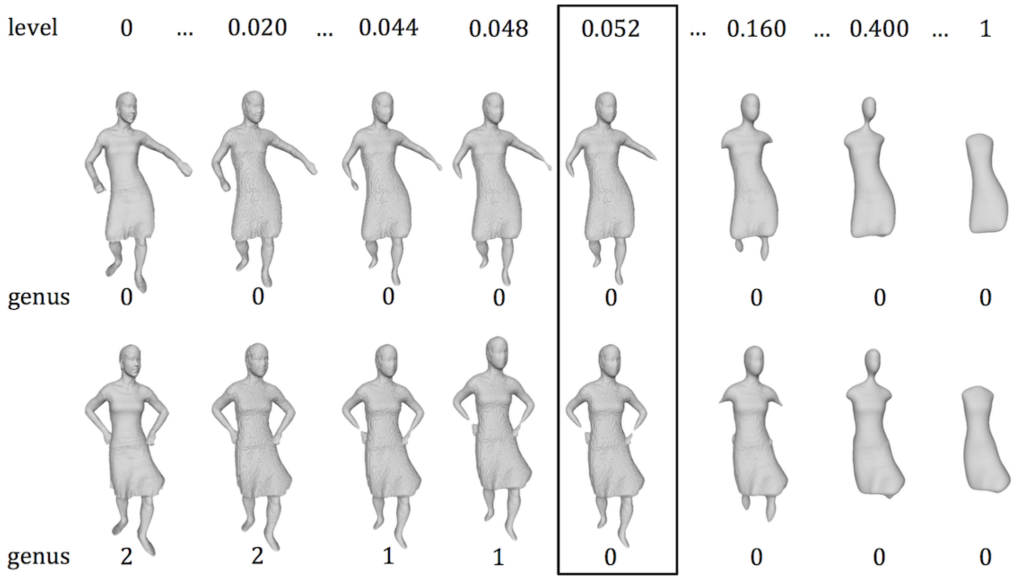


Figure 6.4: Topology equating process involves extracting a collection of deflations for each shape and choosing a level at which the deflations have comparable topology. For this example, the selected level is $0.052$ at which the genus number becomes the same for the deflations of both shapes.

### 6.2.4 Comparison to Preliminary Work [16]

We compare $\rho^0$ with the smooth function used in Genctav et al. [16] in terms of the number of deflation steps needed for obtaining topologically comparable forms of the input shapes. We use a set of 99 topologically different pairs of shapes from SHREC11 robustness benchmark [13]. The deflation at step $k$ is obtained as the iso-surface of the corresponding function at level $0.004 \times k$ where each function is normalized to have the maximum value of 1. The average number of deflation steps is around $2 \pm 7.7$ using $\rho^0$ whereas it is around $6 \pm 14.3$ using the function in Genctav et al. [16]. We find that the topology equating process takes less number of steps when we use $\rho^0$ to extract shape deflations.

The advantage of restricting the collection of deflations via the barrier structure can be illustrated via the following example. Consider a pair of cat models each with links between different shape regions as well as a hole in the main body close to the hip section. The links are removed in early stages of the deflation process whereas the hole is retained until very late stages. Accordingly, the genus number becomes $1$ after

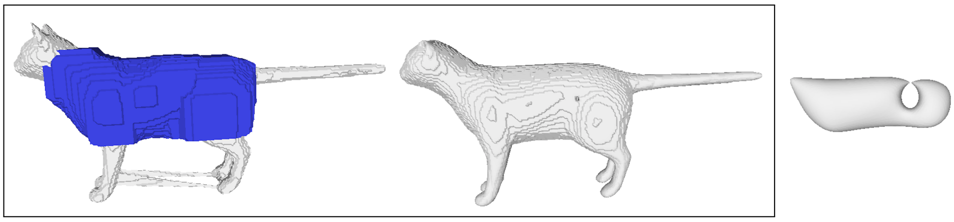

Figure 6.5: (Left) Barrier structure for a cat shape with topological noise. (Middle) Deflation selected by our proposed topology equating strategy which uses the barrier structure. (Right) Deflation selected by Genctav et al. [16].

Figure 6.6: A pair of shapes from i3DPost Multi-view Human Action dataset [19] where 3D models are reconstructed using [36].

a few steps but it reduces to $0$ when the deflation process breaks apart the hole meaning that the essential structures such as the head, legs and tail are already removed. By utilizing the barrier structure in Figure 6.5 (left), our proposed topology equating strategy stops the deflation process before the removal of the hole and, hence, utilizes the pair of deflations with genus number $1$ at the first smallest level (see Figure 6.5 (middle)). In Genctav et al. [16], the collection of deflations is not restricted so it includes all the deflations until the whole shape vanishes. Accordingly, the selected pair of deflations with the smallest genus number becomes the core regions of the shapes with genus number $0$ after the removal of the holes (see Figure 6.5 (right)).

We use the central structure for scale normalization. It gives more reliable normalization as compared to geodesic distances which may be misleading in the case of topological deformations. For example, consider a pair of human shapes one of which has arms fully touching the body (see Figure 6.6). In this case, the respective maximum geodesic distances for the two shapes are not semantically equivalent. For the left shape, it is from hand to foot. For the right shape, it is from head to foot. Hence normalization with respect to maximum geodesic distance is not appropriate.

### 6.3 Experimental Evaluation

In order to evaluate our proposed method that brings a pair of shapes into topologically comparable form via deflating the shape boundary, we use it in a matching task. We transfer the mapping computed between the selected pair of deflations to the input shapes by finding the vertices closest to the matched points of the deflations.

We experiment with the following datasets: the samba sequence from MIT [42], SHREC10 correspondence [12] and SHREC11 robustness [13] benchmarks and the flashkick sequence [36] from University of Surrey.

The samba sequence contains sequences of dancing woman captured using a multi-camera system. Topological differences arise when the arms touch the body during motion. We illustrate our method on a topologically different shape pair from the sequence.

SHREC10 correspondence benchmark includes three objects. Each object comes with a base shape model and five additional forms obtained via isometric deformation of the base shape further deformed by adding topological noise of increasing strength. In our experiments, we match each base shape to the remaining five.

SHREC11 robustness benchmark contains twelve different shape models. For each model, there is one base shape, one isometric shape and five shapes with increasing degree of topological noise. We use a subset for which the ground truth correspondence is available.

The flashkick sequence of a dancing man contains 3D shapes (meshes) captured using multi-camera systems. Topological differences arise when the limbs of the dancer touch each other or the body during motion. We consider three different shape pairs from this sequence in order to illustrate the limitation of our approach.

We follow the same experimental steps in Genctav et al. [16]: We visually compare matching results and quantify matching error or goodness via several measures. The matching error denoted by $\widetilde{D}_{\text{grd}}$ is a normalized deviation from the ground truth correspondence. The lower the $\widetilde{D}_{\text{grd}}$, the better the match. Given a mapping $f$ obtained between sample points of two shapes, the deviation from the ground truth correspondence $g$ is computed as average of the geodesic distances between the points $f(s_i)$ and $g(s_i)$ on the second shape where $s_i$ denotes $i$th sample point of the first shape. The normalization is performed by dividing the deviation to the sampling radius. $\widetilde{D}_{\text{grd}} \leq 1$ holds for the optimal mapping since it means that the deviation from the ground truth correspondence is within the sampling radius. We report several statistics on $\widetilde{D}_{\text{grd}}$. Also, as a discrete measure of goodness, we count the number of matching results for which $\widetilde{D}_{\text{grd}}$ is less than $1$. The larger this count, the more successful is the matching approach. The matching results are also compared with biharmonic-based mapping in which shapes are matched without deflation using biharmonic distance [25]. Note that biharmonic distance is a diffusion-based distance measure which is robust to small topological noise.

## 6.4 Results and Discussion

### 6.4.1 Samba Sequence

For the pair in Figure 6.1 the matching result is visually presented in Figure 6.7 (a). The input meshes represent the visual hull of the two shapes obtained by a simple voxel carving algorithm. The models have different topologies as arms of the second shape touch the body. Our approach utilizes topologically similar representations of the input shapes and provides a mapping between the deflated forms of the input models which are the iso-surfaces at $\ell = 0.052$. The topological similarity between the deflations enables the correct mapping for which $\widetilde{D}_{\text{grd}}$ is $0.85$. For comparison, the biharmonic distance based mapping without deflation is given in Figure 6.7 (b) where the right arm of the first model is matched to the head of the second one increasing $\widetilde{D}_{\text{grd}}$ to $2.82$.

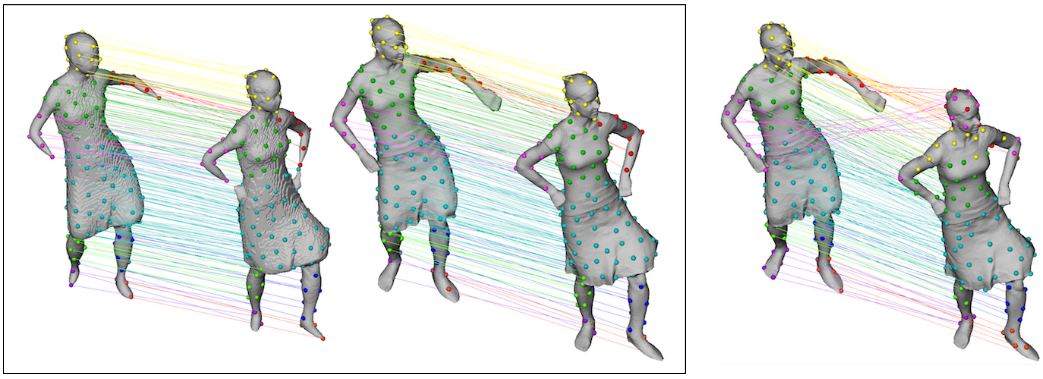

(a) (b)

Figure 6.7: (a) Mapping between iso-surfaces at $\ell = 0.052$ (first) and its transfer to the input shapes (second). (b) Biharmonic-based mapping.

### 6.4.2 SHREC10

We search a match between each base shape and each of its five deformations containing topological noise. The topological noise is caused by the edge links between different parts of the shapes. We examine the performance of the proposed approach in comparison with the biharmonic-based mapping while the noise strength increases. In Table 6.2, we present average of $\widetilde{D}_{\mathrm{grd}}$ over the obtained results where the highest topology noise strength is different for the pairs considered at each row. The biharmonic-based mapping diverges from being optimal when the noise strength is greater than three. Our proposed approach is robust to the topological noise as all of the mappings are very close to the optimal and it performs the best for all of the experiments. In Figure 6.8, we show the matching result obtained by our method for two human shapes where the model of the sitting man has topological noise of degree five caused by the edge links between the hands and the legs.

Table 6.2: Performance of the proposed approach in comparison with the biharmonic-based mapping using SHREC10 correspondence benchmark. The results represent average of $\widetilde{D}_{\mathrm{grd}}$ over the mappings. The highest topology noise strength is different for the pairs considered at each row.

| max noise strength | biharmonic | proposed |
|---|---|---|
| 1 | 1.67 | **1.11** |
| 2 | 1.69 | **1.12** |
| 3 | 1.70 | **1.12** |
| 4 | 2.22 | **1.12** |
| 5 | 2.53 | **1.12** |

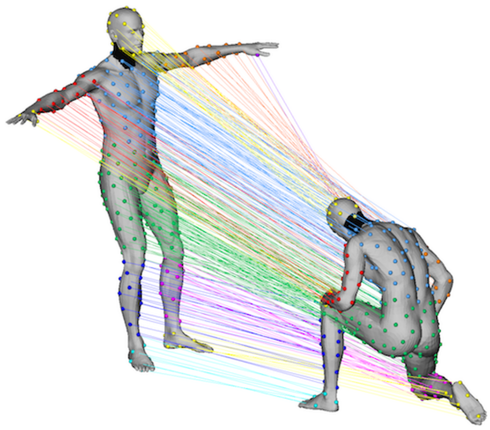

Figure 6.8: Mapping obtained by our method for two shapes from SHREC10 correspondence benchmark where model of the sitting man has topological noise of degree five.

### 6.4.3 SHREC11

We use the shape models 0002, 0004, 0005, 0007, 0008, 0012 and 0014 for which the ground truth correspondence is available. We use the isometric shape and five shapes with topology noise from each model. We also use the base shape from the models 0002 and 0007. In Figure 6.9, we present $\widetilde{D}_{\mathrm{grd}}$ for the mappings obtained using the proposed approach and the biharmonic-based mapping. The input pairs are the shapes from each model where at least one of them has topological distortion. Note that we do not present $\widetilde{D}_{\mathrm{grd}}$ for some of the mappings where the symmetric flip problem arises. The number of pairs with the symmetric flip problem is $3$ for the proposed method and $12$ for the biharmonic mapping. As shown in Figure 6.9 and summarized in Table 6.3, our approach successfully handles the topology noise as almost all of our mappings are optimal ($\widetilde{D}_{\mathrm{grd}} \leq 1$). Excluding the mappings with symmetric flip, average of $\widetilde{D}_{\mathrm{grd}}$ over all results, $\mathrm{avg}(\widetilde{D}_{\mathrm{grd}})$, is very small for our method compared to the biharmonic-based mapping (see Table 6.3). In Figure 6.10, we present the mappings obtained by the proposed approach for three pairs of shapes.

Finally, we present a visual comparison of our approach with the method [26] which performed the best in the topology noise category of SHREC10 correspondence benchmark. We run the method [26] on a pair of horse shapes from SHREC11 robustness benchmark using its code available on the web. One of the horse shapes has the topological noise as its back legs are linked to each other. Figure 6.11 shows that our approach successfully handles the topology noise whereas [26] fails to solve the correspondence problem under the given topology noise.

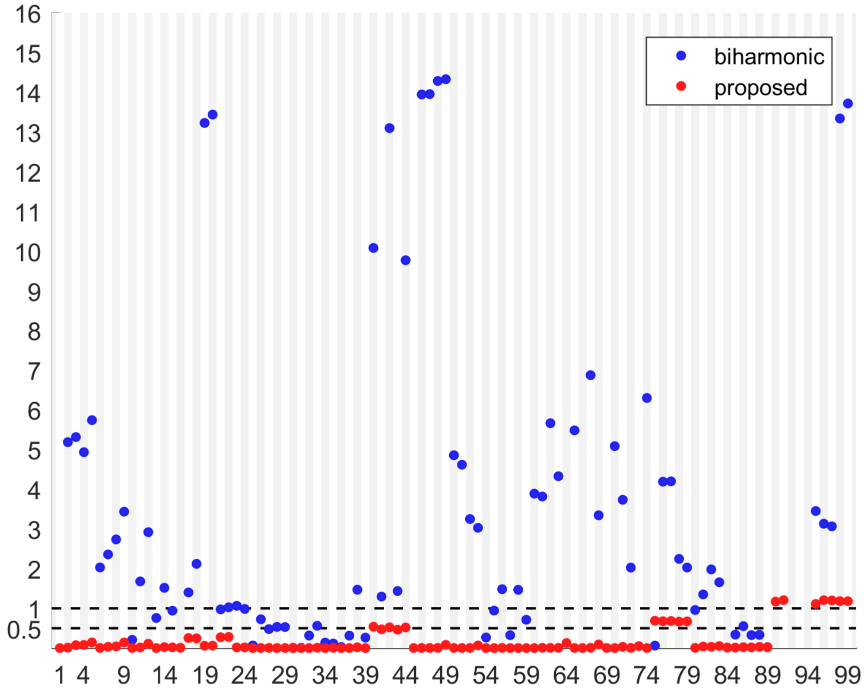


Figure 6.9: Normalized average ground truth error $\widetilde{D}_{\text{grd}}$ for the mappings between topologically different pairs of shapes from SHREC11 robustness benchmark. The errors in blue color are obtained using biharmonic-based mapping. The errors in red color shows the performance of the proposed approach. $\widetilde{D}_{\text{grd}}$ is not presented for some of the mappings where the symmetric flip problem arises.

Table 6.3: Summary of the results in Figure 6.9. Performance of the proposed approach in comparison with the biharmonic-based mapping using SHREC11 robustness benchmark.

| | biharmonic | proposed |
|---|---|---|
| # of $\widetilde{D}_{\text{grd}} \leq 1$ | 31 | 89 |
| $\text{avg}(\widetilde{D}_{\text{grd}})$ | 3.45 | 0.18 |
| $\text{stddev}(\widetilde{D}_{\text{grd}})$ | 4.08 | 0.34 |
| $\min(\widetilde{D}_{\text{grd}})$ | 0.01 | 0 |
| $\max(\widetilde{D}_{\text{grd}})$ | 14.32 | 1.21 |

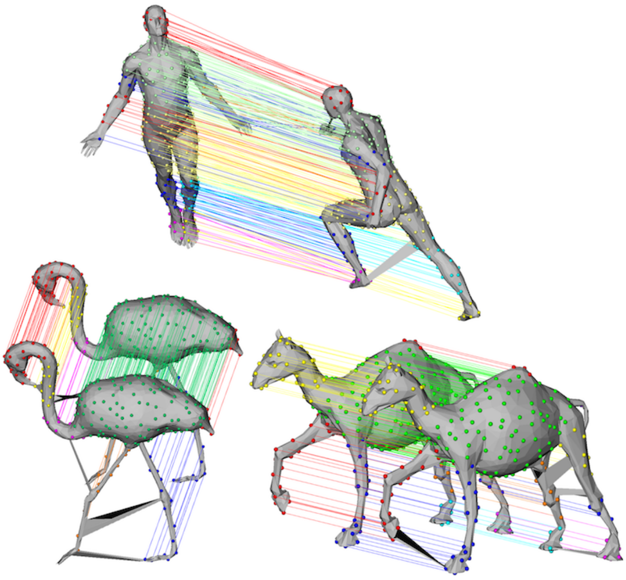

Figure 6.10: Mappings obtained by the proposed approach for three pairs of shapes from SHREC11 robustness benchmark.

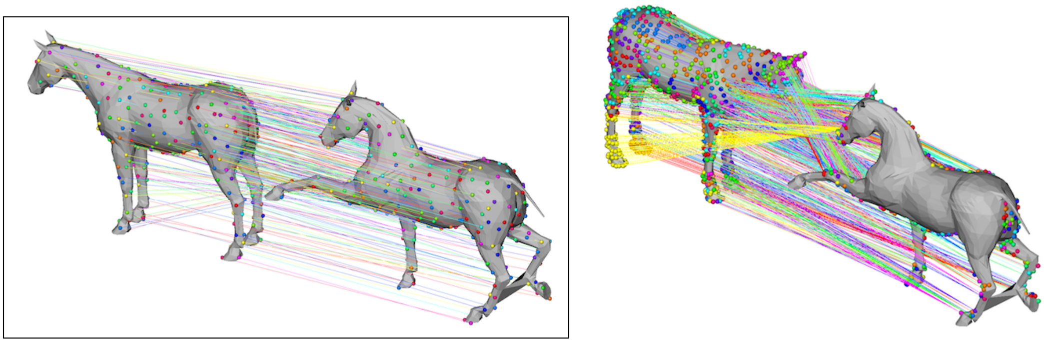

Figure 6.11: For a pair of shapes from SHREC11 robustness benchmark (Left) Mapping result obtained by the proposed approach (Right) Dense mapping result obtained by the method [26].

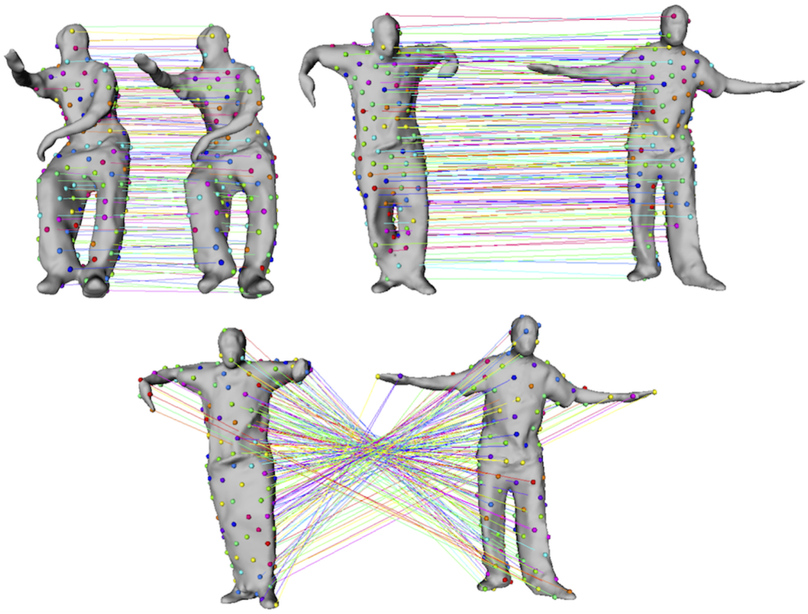

Figure 6.12: Mappings obtained by the proposed approach for three different pairs of shapes from the flashkick sequence [36].

### 6.4.4 Flashkick Sequence

In Figure 6.12, we present the mappings obtained using our approach between three different pairs of shapes from the flashkick sequence [36]. For the pair on the top left, our approach performs well since the topological noise is caused by localized touches i.e. foot-to-foot and hand-to-leg connection in the first and the second shape, respectively. The pair on the top right represents an input case where our approach starts to fail where the legs in the first shape are merged along their bottom half. The degradation of the matching result, which is especially around the legs, is due to that the topological difference is resolved when the thinner leg is split by the deflations. For the pair at the bottom, our approach results in an incorrect mapping since the corresponding topological difference, which is due to full merge of the legs in the first shape, cannot be removed via deflating the shape boundary.

# CHAPTER 7

# SUMMARY AND CONCLUSION

In this thesis, using an elliptic PDE or its modifications, we developed several shape fields each providing a different shape characterization.

First, we compared two solutions of the elliptic PDE, one solved on the shape domain and the other one solved on a reference disk. This way, we indirectly measured the deviation of the local configuration of each shape point from the reference disk. We called the shape field composed of these local deviation measures as discrepancy. We showed that discrepancy provides a rich shape representation. We used its entropy for global shape characterization, its probability distribution as a descriptor for context-dependent categorization, and its sign for binary shape domain labeling.

Second, we solved the elliptic PDE multiple times by varying either the diffusion parameter or the right hand side function and constructed high-dimensional feature representation of the shape points. By applying a data analysis tool on the constructed feature space, we determined the distinctness of each shape point. The distinctness values obtained by varying the diffusion parameter are used for representing 2D articulated shapes. We partitioned the shape into a set of regions via the spatial distribution of the distinctness and represented each region by the normalized distinctness histogram. Using such a representation that does not involve modeling relations of shape components, we obtained a clustering performance comparable to structural methods. The distinctness values obtained by varying the right hand side function are used as a measure of saliency over the surfaces of 3D shapes. By varying the parameter of the data analysis tool, we obtained multiple saliency measures each emphasizing different shape structures. For the smallest value of the parameter, the global shape structures are found to be salient. As the parameter increases, we obtained a saliency measure that has a larger value only on the local structures. The multiple saliency measures can be used for further shape processing. As an example, we grouped the surface points by combining the multiple saliency measures.

Third, we considered modifications of the elliptic PDE and obtained a pair of shape fields. The first field provided adaptive deflations of the shape surface and the second field provided a central barrier structure for stopping the adaptive deflations. Using these two fields, we developed a topology equating process for a pair of 3D shapes.

# REFERENCES


[1] N. Ahmed, C. Theobalt, C. Rossl, S. Thrun, and H. Seidel. Dense correspondence finding for parametrization-free animation reconstruction from video. In *Proc. of Computer Vision and Pattern Recognition, CVPR*, 2008.

[2] M. A. Aktas and J. Zunic. A family of shape ellipticity measures for galaxy classification. *SIAM Journal on Imaging Sciences*, 6(2):765–781, 2013.

[3] S. Almeida-Prieto, J. Blanco-Méndez, and F. J. Otero-Espinar. Image analysis of the shape of granulated powder grains. *Journal of Pharmaceutical Sciences*, 93(3):621–634, 2004.

[4] C. Aslan, A. Erdem, E. Erdem, and S. Tari. Disconnected skeleton: shape at its absolute scale. *IEEE Trans. on Pattern Anal. and Mach. Intell.*, 30(12):2188–2203, 2008.

[5] C. Aslan and S. Tari. An axis-based representation for recognition. In *Proc. of International Conference on Computer Vision, ICCV*, 2005.

[6] F. Attneave. Some informational aspects of visual perception. *Psychology Review*, 61(3):183–193, 1954.

[7] F. Attneave. Physical determinants of the judged complexity of shape. *J. of Experimental Psychology*, 53(4):221–227, 1957.

[8] S. Bai, Z. Liu, and X. Bai. Co-spectral for robust shape clustering. *Pattern Recognition Letters*, 83:388–394, 2016.

[9] X. Bai and L. Latecki. Path similarity skeleton graph matching. *IEEE Trans. on Pattern Anal. and Mach. Intell.*, 30(7):1282–1292, 2008.

[10] E. Baseski, A. Erdem, and S. Tari. Dissimilarity between two skeletal trees in a context. *Pattern Recognition*, 42(3):370–385, 2009.

[11] S. Belongie, J. Malik, and J. Puzicha. Shape matching and object recognition using shape contexts. *IEEE Trans. on Pattern Anal. and Mach. Intell.*, 24(4):509–522, 2002.

[12] A. Bronstein, M. Bronstein, U. Castellani, A. Dubrovina, L. Guibas, R. Horaud, R. Kimmel, D. Knossow, E. Von Lavante, D. Mateus, M. Ovsjanikov, and A. Sharma. SHREC 2010: robust correspondence benchmark. In *Proc. Eurographics Workshop on 3D Object Retrieval*, 2010.

[13] A. Bronstein, M. Bronstein, U. Castellani, B. Falcidieno, A. Fusiello, A. Godil, L. Guibas, I. Kokkinos, Z. Lian, M. Ovsjanikov, G. Patane, M. Spagnuolo, and R. Toldo. SHREC 2010: robust large-scale shape retrieval benchmark. In *Proc. Eurographics Workshop on 3D Object Retrieval*, 2010.

[14] A. Bronstein, M. Bronstein, R. Kimmel, M. Mahmoudi, and G. Sapiro. A Gromov-Hausdorff framework with diffusion geometry for topologically-robust non-rigid shape matching. *International Journal of Computer Vision*, 89(2):266–286, 2010.

[15] B. J. Frey and D. Dueck. Clustering by passing messages between data points. *Science*, 315(5814):972–976, 2007.

[16] A. Genctav, Y. Sahillioglu, and S. Tari. 3D shape correspondence under topological noise. In *24th Signal Processing and Communication Application Conference, SIU*, 2016.

[17] A. Genctav and S. Tari. Discrepancy: Local/global shape characterization with a roundness bias. *Journal of Mathematical Imaging and Vision*, 2018. doi:10.1007/s10851-018-0851-8.

[18] M. Genctav, A. Genctav, and S. Tari. Nonlocal via local–nonlinear via linear: A new part-coding distance field via screened Poisson equation. *J. Math. Imaging Vis.*, 55(2):242–252, 2016.

[19] N. Gkalelis, H. Kim, A. Hilton, N. Nikolaidis, and I. Pitas. The i3DPost multi-view and 3D human action/interaction. In *Proc. CVMP*, 2009.

[20] A. M. Herrera-Navarro, H. Jimenez-Hernandez, and I. R. Terol-Villalobos. A probabilistic measure of circularity. In *Combinatorial Image Analysis*, pages 75–89. Springer, 2012.

[21] L. Latecki, R. Lakamper, and T. Eckhardt. Shape descriptors for non-rigid shapes with a single closed contour. In *Proc. of Computer Vision and Pattern Recognition, CVPR*, 2000.

[22] C. H. Lee, A. Varshney, and D. W. Jacobs. Mesh saliency. *ACM Trans. Graph.*, 24(3):659–666, 2005.

[23] Z. Lin, M. Chen, and Y. Ma. The augmented Lagrange multiplier method for exact recovery of corrupted low-rank matrices. *arXiv preprint arXiv:1009.5055*, 2010.

[24] H. Ling and D. W. Jacobs. Shape classification using the inner-distance. *IEEE Trans. on Pattern Anal. and Mach. Intell.*, 29(2):286–299, 2007.

[25] Y. Lipman, R. Rustamov, and T. Funkhouser. Biharmonic distance. *ACM Trans. Graph.*, 29(3):27:1–27:11, 2010.

[26] D. Mateus, R. Horaud, D. Knossow, F. Cuzzolin, and E. Boyer. Articulated shape matching using Laplacian eigenfunctions and unsupervised point registration. In *Proc. of Computer Vision and Pattern Recognition, CVPR*, 2008.

[27] C. R. Maurer, R. Qi, and V. Raghavan. A linear time algorithm for computing exact euclidean distance transforms of binary images in arbitrary dimensions. *IEEE Trans. on Pattern Anal. and Mach. Intell.*, 25(2):265–270, 2003.

[28] K. Misztal and J. Tabor. Ellipticity and circularity measuring via Kullback-Leibler divergence. *J. Math. Imaging Vis.*, 55(1):136–150, 2016.

[29] M. Ovsjanikov, Q. Merigot, F. Memoli, and L. Guibas. One point isometric matching with the heat kernel. *Comput. Graph. Forum*, 29(5):1555–1564, 2010.

[30] Z. Pincus and J. A. Theriot. Comparison of quantitative methods for cell-shape analysis. *Journal of Microscopy*, 227(2):140–156, 2007.

[31] P. L. Rosin. Measuring shape: ellipticity, rectangularity, and triangularity. *Machine Vision and Applications*, 14(3):172–184, 2003.

[32] A. D. Santis, O. D. Bartolomeo, D. Iacoviello, and F. Iacoviello. Quantitative shape evaluation of graphite particles in ductile iron. *Journal of Materials Processing Technology*, 196(1):292–302, 2008.

[33] A. Sharma and R. Horaud. Shape matching based on diffusion embedding and on mutual isometric consistency. In *Proc. of Computer Vision and Pattern Recognition Workshops*, 2010.

[34] A. Sharma, R. Horaud, J. Cech, and E. Boyer. Topologically-robust 3D shape matching based on diffusion geometry and seed growing. In *Proc. of Computer Vision and Pattern Recognition, CVPR*, 2011.

[35] W. Shen, Y. Wang, X. Bai, H. Wang, and L. Latecki. Shape clustering: Common structure discovery. *Pattern Recognition*, 46(2):539–550, 2013.

[36] J. Starck and A. Hilton. Surface capture for performance based animation. *IEEE Computer Graphics and Applications*, 27(3):21–31, 2007.

[37] S. Tari. Extracting parts of 2D shapes using local and global interactions simultaneously. In C. Chen, editor, *Handbook of Pattern Recognition and Computer Vision, 4th edn.*, pages 283–303, 2009.

[38] S. Tari. Hierarchical shape decomposition via level sets. In *ISMM*, 2009.

[39] S. Tari and M. Genctav. From a non-local Ambrosio-Tortorelli phase field to a randomized part hierarchy tree. *J. Math. Imaging Vis.*, 49(1):69–86, 2014.

[40] S. Tari, J. Shah, and H. Pien. A computationally efficient shape analysis via level sets. In *IEEE Workshop on Mathematical Methods in Biomedical Image Analysis*, 1996.

[41] L. van der Maaten and G. Hinton. Visualizing high-dimensional data using t-SNE. *J. Mach. Learn. Res.*, 9:2579–2605, 2008.

[42] D. Vlasic, I. Baran, W. Matusik, and J. Popovic. Articulated mesh animation from multi-view silhouettes. *ACM Trans. Graph.*, 27(3):97:1–97:9, 2008.

[43] J. D. Winter and J. Wagemans. Perceptual saliency of points along the contour of everyday objects: a large-scale study. *Percept. Psychophys.*, 70(1):50–64, 2008.

[44] X. Zhang, X. Le, A. Panotopoulou, E. Whiting, and C. C. L. Wang. Perceptual models of preference in 3d printing direction. *ACM Trans. Graph.*, 34(6):215:1–215:12, 2015.

[45] J. Zunic, K. Hirota, and P. L. Rosin. A Hu moment invariant as a shape circularity measure. *Pattern Recognition*, 43(1):47–57, 2010.

# APPENDIX A

# EK A

## A.1 Numerical Implementation of the PDEs (1.1), (1.6), and (1.8)

To compute the numerical solution on the arbitrary shape domain, we discretize the PDEs on a standard grid via finite-difference method. The discretization yields a linear system of equations with sparse and symmetric positive definite system matrix. There is a plethora of direct and iterative alternatives to solve this system. We used a direct solver based on Cholesky factorization.

The discretization of (1.1) in 2D/3D leads to a linear system of equations in which each pixel/voxel is related with its neighbors as follows:

$$\begin{aligned} v_{x+1,y} + v_{x-1,y} + v_{x,y+1} + v_{x,y-1} - (4+a^2)\,v_{x,y} &= 0 \\ v_{x+1,y,z} + v_{x-1,y,z} + v_{x,y+1,z} + v_{x,y-1,z} + v_{x,y,z+1} + v_{x,y,z-1} - (6+a^2)\,v_{x,y,z} &= 0 \end{aligned} \tag{A.1}$$

where the value of $v$ is taken as 1 for the pixels/voxels outside the shape domain.

The discretization of (1.6) in 2D/3D:

$$\begin{aligned} v_{x+1,y} + v_{x-1,y} + v_{x,y+1} + v_{x,y-1} - (4+a^2)\,v_{x,y} &= -1 \\ v_{x+1,y,z} + v_{x-1,y,z} + v_{x,y+1,z} + v_{x,y-1,z} + v_{x,y,z+1} + v_{x,y,z-1} - (6+a^2)\,v_{x,y,z} &= -1 \end{aligned} \tag{A.2}$$

where the value of $v$ is taken as 0 for the pixels/voxels outside the shape domain.

The discretization of (1.8) in 2D/3D:

$$\begin{aligned} v_{x+1,y} + v_{x-1,y} + v_{x,y+1} + v_{x,y-1} - (4+a^2)\,v_{x,y} &= -f_{x,y} \\ v_{x+1,y,z} + v_{x-1,y,z} + v_{x,y+1,z} + v_{x,y-1,z} + v_{x,y,z+1} + v_{x,y,z-1} - (6+a^2)\,v_{x,y,z} &= -f_{x,y,z} \end{aligned} \tag{A.3}$$

where the value of $v$ is taken as 0 for the pixels/voxels outside the shape domain.

## CURRICULUM VITAE

### PERSONAL INFORMATION

**Surname, Name:** Gençtav, Aslı

**Nationality:** Turkish (TC)

**Date and Place of Birth:** 21.02.1985, Ankara

**Marital Status:** Married

**Phone:** 0 531 2719860

### EDUCATION

| Degree | Institution | Year of Graduation |
|---|---|---|
| M.S. | Bilkent University | 2010 |
| B.S. | Middle East Technical University | 2007 |
| High School | İstanbul Atatürk Fen Lisesi | 2002 |

### PROFESSIONAL EXPERIENCE

| Year | Place | Enrollment |
|---|---|---|
| 2013-2014 | HAVELSAN Inc. | Senior Software Engineer |
| 2009-2013 | Middle East Technical University | Teaching Assistantship |
| 2007-2009 | Bilkent University | Teaching and Research Assistantship |

## PUBLICATIONS

### Books

Research in Shape Analysis. A. Genctav, K. Leonard, S. Tari, E. Hubert, G. Morin, N. El-Zehiry, E. Chambers (eds.), Association for Women in Mathematics Series, vol 12, Springer, 2018

### Book Chapters

A. Genctav, M. Genctav, S. Tari, A Non-local Measure for Mesh Saliency via Feature Space Reduction, *accepted*

A. Genctav, S. Tari, Adaptive Deflation Stopped by Barrier Structure for Equating Shape Topologies Under Topological Noise, in: *A. Genctav et al. (eds) Research in Shape Analysis*, Association for Women in Mathematics Series, vol 12, Springer, 2018

### International Journal Publications

A. Genctav, S. Tari, A Non-structural Representation Scheme for Articulated Shapes, *submitted*

A. Genctav, S. Tari, Discrepancy - Local/Global Shape Characterization with a Roundness Bias, *Journal of Mathematical Imaging and Vision*, 2018, doi:10.1007/s10851-018-0851-8

M. Genctav, A. Genctav, S. Tari, NonLocal via Local-NonLinear via Linear: A New Partcoding Distance Field via Screened Poisson Equation, *Journal of Mathematical Imaging and Vision*, 55(2):242–252, June 2016

A. O. Akyuz, A. Genctav, A reality check for radiometric camera response recovery algorithms, *Computers & Graphics*, 37(7):935–943, November 2013

A. Genctav, S. Aksoy, S. Onder, Unsupervised Segmentation and Classification of

Cervical Cell Images, *Pattern Recognition*, 45(12):4151–4168, December 2012

### International Conference Publications

A. Genctav, S. Tari, A Product Shape Congruity Measure via Entropy in Shape Scale Space, *EUSIPCO 2017 Satellite Workshops*, Kos Island, Greece, September 2017

A. Genctav, A. O. Akyuz, Evaluation of radiometric camera response recovery methods, *SIGGRAPH Asia 2011 Posters*, Hong Kong, 2011

A. Kale, S. Aksoy, Segmentation of Cervical Cell Images, *20th IAPR International Conference on Pattern Recognition*, Istanbul, August 2010

D. Zamalieva, F. Kalaycilar, A. Kale, S. Pehlivan, F. Can, Stylistic Document Retrieval for Turkish, *24th International Symposium on Computer and Information Sciences*, Northern Cyprus, September 2009

F. Kalaycilar, A. Kale, D. Zamalieva, S. Aksoy, Mining of Remote Sensing Image Archives Using Spatial Relationship Histograms, *IEEE International Geoscience and Remote Sensing Symposium (IGARSS 2008)*, Boston, July 2008

### National Conference Publications

A. Genctav, Y. Sahillioglu, S. Tari, Topolojik Gürültü Altında 3B Şekil Eşleme, *IEEE Sinyal Işleme ve Uygulamaları Kurultayı (SIU 2016)*, Zonguldak, Mayıs 2016

A. Kale, S. Aksoy, S. Onder, Pap Smear Test Görüntülerinde Hücre Çekirdeklerinin Bölütlenmesi, *IEEE Sinyal Işleme ve Uygulamaları Kurultayı (SIU 2009)*, Antalya, Nisan 2009

### Awards

*PhD Scholarship*, The Scientific and Technological Research Council of Turkey (TUBITAK)

*MSc Scholarship*, The Scientific and Technological Research Council of Turkey (TUBITAK)

## Professional Activities

*Workshop Organizer*, EUSIPCO 2017 Satellite Workshop on Creative Design and Advanced Manufacturing: An emerging application area for Signals and Systems, Kos Island, Greece, September 2, 2017

*Organizer*, WiSh Special Session: Shape Modeling and Applications, AWM Research Symposium 2017, University of California Los Angeles, USA, April 8, 2017

*Workshop Organizer*, A Collaborative Research Workshop: Women in Shape-2: Modeling Boundaries of Objects in 2- and 3-Dimensions, Sirince, Turkey, June 6–12, 2016

*Administrative Assistant*, Computational Problems in Creative Design with Shapes, MIT, USA, June 12–13, 2015

*Administrative Assistant*, SIGGRAPH Asia 2014 Workshop on Creative Shape Modeling and Design, Shenzhen, China, December 3, 2014